CrossMark

J. Fluid Mech. (2005), *vol.* 522, *pp.* 179–214. © 2005 Cambridge University Press
DOI: 10.1017/S0022112004001880 Printed in the United Kingdom

Regular shock refraction at an oblique planar density interface in magnetohydrodynamics

By V. WHEATLEY[1], D. I. PULLIN[1] AND R. SAMTANEY[2]

[1]Graduate Aeronautical Laboratories, 301-46, California Institute of Technology, Pasadena, CA 91125, USA

[2]Princeton Plasma Physics Laboratory, Princeton University, Princeton, NJ 08543, USA

(Received 10 November 2003 and in revised form 2 July 2004)

We consider the problem of regular refraction (where regular implies all waves meet at a single point) of a shock at an oblique planar contact discontinuity separating conducting fluids of different densities in the presence of a magnetic field aligned with the incident shock velocity. Planar ideal magnetohydrodynamic (MHD) simulations indicate that the presence of a magnetic field inhibits the deposition of vorticity on the shocked contact. We show that the shock refraction process produces a system of five to seven plane waves that may include fast, intermediate, and slow MHD shocks, slow compound waves, 180° rotational discontinuities, and slow-mode expansion fans that intersect at a point. In all solutions, the shocked contact is vorticity free and hence stable. These solutions are not unique, but differ in the types of waves that participate. The set of equations governing the structure of these multiple-wave solutions is obtained in which fluid property variation is allowed only in the azimuthal direction about the wave-intersection point. Corresponding solutions are referred to as either quintuple-points, sextuple-points, or septuple-points, depending on the number of participating waves. A numerical method of solution is described and examples are compared to the results of numerical simulations for moderate magnetic field strengths. The limit of vanishing magnetic field at fixed permeability and pressure is studied for two solution types. The relevant solutions correspond to the hydrodynamic triple-point with the shocked contact replaced by a singular structure consisting of a wedge, whose angle scales with the applied field magnitude, bounded by either two slow compound waves or two 180° rotational discontinuities, each followed by a slow-mode expansion fan. These bracket the MHD contact which itself cannot support a tangential velocity jump in the presence of a non-parallel magnetic field. The magnetic field within the singular wedge is finite and the shock-induced change in tangential velocity across the wedge is supported by the expansion fans that form part of the compound waves or follow the rotational discontinuities. To verify these findings, an approximate leading-order asymptotic solution appropriate for both flow structures was computed. The full and asymptotic solutions are compared quantitatively.

1. Introduction

Samtaney (2003) has demonstrated, via numerical simulations, that the growth of the Richtmyer–Meshkov instability is suppressed in the presence of a magnetic field. The particular flow studied was that of a shock interacting with an oblique planar contact discontinuity (CD) separating conducting fluids of different densities within the framework of strongly planar ideal magnetohydrodynamics (MHD). Here, we define a flow to be *planar* if there are no derivatives in the out-of-plane (z) direction,

https://doi.org/10.1017/S0022112004001880 Published online by Cambridge University Press

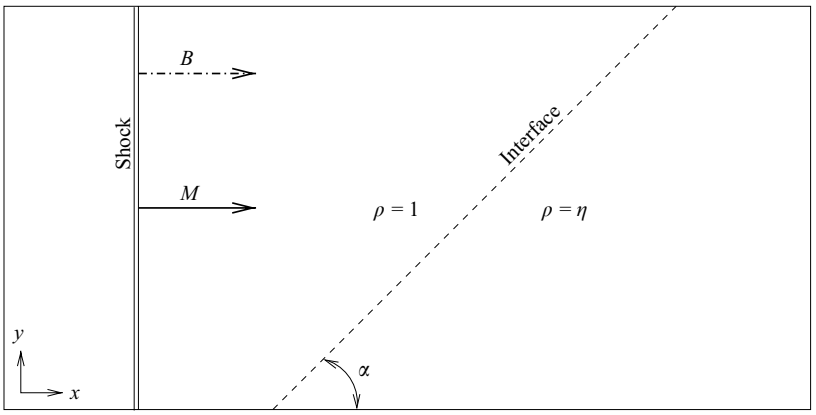


FIGURE 1. Physical set-up for the Richtmyer–Meshkov simulations of Samtaney (2003). The initial pressure in the unshocked regions is $p_0 = 1$. Symmetry boundary conditions are applied in the vertical direction.

and *strongly planar* if there is also a reference frame in which there are no vector components in the z-direction. The physical set-up for the shock interaction problem is depicted in figure 1. The applied magnetic field is aligned with the motion of the incident shock. This flow is characterized by five dimensionless parameters: the incident shock *sonic* Mach number M, the density ratio across the interface η, the angle between the incident shock normal and the interface α, the non-dimensional strength of the applied magnetic field $\beta^{-1} = B^2/2\mu_0 p_0$, and the ratio of specific heats γ. Here, the magnitude of the applied magnetic field B is made dimensionless against the square root of the product of the permeability μ_0 and the pressure p_0 of the gas. Samtaney presented detailed numerical results for cases with $M = 2$, $\eta = 3$, $\alpha = \pi/4$, $\beta^{-1} = 0$ (no magnetic field) or 0.5 (magnetic field present), and $\gamma = 1.4$. Figure 2 shows the density fields for these two cases after the incident shock has passed through the interface. For the case with no applied magnetic field, vorticity is deposited on the interface during the shock interaction. The interface is then a vortex layer and rolls up through local Kelvin–Helmholtz instability. For the case with an applied magnetic field, the interface remains smooth and no roll-up is observed, indicating that the instability is suppressed (Samtaney 2003).

The suppression of the instability can be understood by examining how the shock refraction process at the interface changes with the application of a magnetic field. For the case with no applied magnetic field, $\beta^{-1} = 0$, the details of the shock refraction process are shown in figure 3(a). The velocity vectors shown are in the reference frame where the point of intersection between the shocks and the interface is stationary. For Samtaney's choice of parameters, the incident shock I is transformed into a reflected shock R and a transmitted shock T. This is the case for all sets of parameters considered here, although other wave configurations involving expansion fans are possible for other parameter sets. The angles of R and T to the flow are such that the flow angles and pressures on either side of the interface are matched. The doubly shocked flow downstream of R has a lower velocity than the flow on the other side of the interface, which has been decelerated only by T, resulting in a shear across the interface. Thus, in the absence of an applied magnetic field, the shock refraction process deposits vorticity on the interface, causing it to roll up owing to local Kelvin–Helmholtz instability.

https://doi.org/10.1017/S0022112004001880 Published online by Cambridge University Press

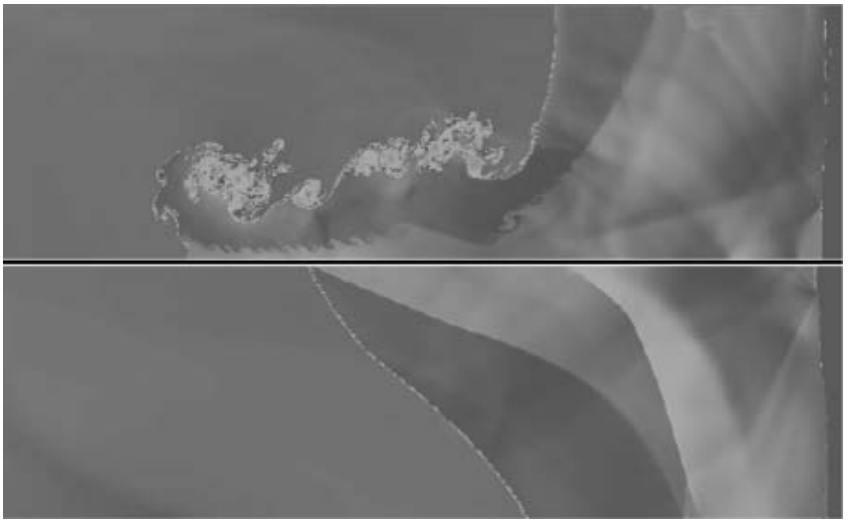


FIGURE 2. Density fields from the Richtmyer–Meshkov simulations of Samtaney (2003) after the incident shock has completely passed through the interface. The initial condition geometry is shown in figure 1. The transmitted shock is located near the right-hand edge of each image. The top image is from a simulation with no magnetic field, while the bottom image is from a simulation where a magnetic field with $\beta = 2$ is present. Note that the vertical coordinate is reversed in the bottom image.

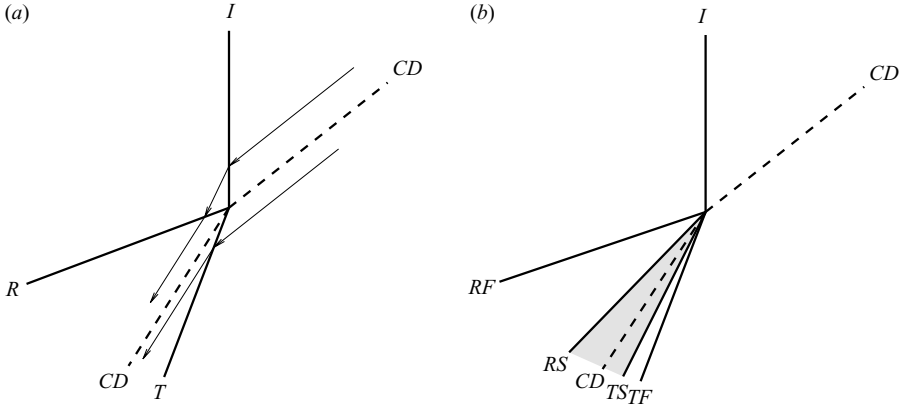


FIGURE 3. (*a*) Triple-point wave structure and streamlines resulting from a shock refraction process with $M = 2$, $\alpha = \pi/4$, and $\eta = 3$ in the absence of an applied magnetic field ($\beta^{-1} = 0$). (*b*) Quintuple-point wave structure resulting from an MHD shock refraction process with $M = 2$, $\alpha = \pi/4$, $\eta = 3$ and $\beta = 2$. *CD*, contact discontinuity; *I*, incident shock; *R*, reflected shock; *RF*, reflected fast wave; *RS*, reflected slow/intermediate wave; *T*, transmitted shock; *TF*, transmitted fast wave; *TS*, transmitted slow/intermediate wave. Shaded area is the inner layer.

In general, this wave configuration is not a valid solution of the equations of ideal MHD if a magnetic field is present. This is because an MHD CD cannot support a jump in either tangential velocity u_t or magnetic field B_t if the magnetic field has a component normal to the discontinuity (see e.g. Sutton & Sherman 1965). Thus, there are four constraints that must be satisfied at the interface: continuous total pressure, flow angle, tangential velocity and tangential magnetic field (the normal magnetic

https://doi.org/10.1017/S0022112004001880 Published online by Cambridge University Press

field must also be continuous, but this is not independent of the other constraints for this flow). There are only two degrees of freedom in the system, the angles of R and T, so that, in general, there is no solution. An exception occurs when the incident shock velocity and the applied magnetic field $\boldsymbol{B}$ are aligned in the reference frame of the intersection point ($\boldsymbol{B}$ is parallel to the density interface). In this case, the MHD Rankine–Hugoniot relations ensure that the magnetic field and velocity vectors will be aligned in all regions of the flow, which allows jumps in u_t and B_t across the CD. Hence, there are two fewer constraints to be satisfied, admitting three-shock solutions to the aligned field shock interaction problem (Ogawa & Fujiwara 1996). Such solutions have been studied in detail by Bestman (1975) and Ogawa & Fujiwara (1996).

In cases where the normal magnetic field B_n at the interface is non-zero, such as the problem under consideration here, a different system of waves must arise from the shock refraction process. From his numerical results, Samtaney (2003) observed that, in the presence of a magnetic field, R and T are replaced by fast magnetosonic shocks, denoted RF and TF, respectively. In addition, the vortex layer bifurcates into a structure that we will call the *inner layer*, which consists of two sub-fast magnetosonic shocks, called RS and TS, respectively, bracketing an MHD CD. This wave configuration is shown in figure 3(*b*) and will hereinafter be referred to as a *quintuple-point*. Note that the presence of shocks RS and TS provides the additional two degrees of freedom necessary to satisfy the two additional constraints at the interface identified by Ogawa & Fujiwara (1996). It is well known that magnetosonic shocks support tangential velocity jumps (see e.g. Sutton & Sherman 1965). This allows shocks RS and TS to eliminate the velocity discrepancy between the flow downstream of shock RF and that downstream of shock TF, leaving the MHD CD vorticity free. Thus, we see that the application of a magnetic field can suppress the Kelvin–Helmholtz instability because, in most cases, the shock refraction process does not deposit vorticity on the density interface.

In the subsequent sections, we demonstrate that the quintuple-point and other similar structures are entropy-satisfying weak solutions of the equations of ideal MHD, and investigate how these solutions converge to the hydrodynamic triple-point as the magnitude of the applied magnetic field B tends to zero. In § 2, we formulate the equations required to solve the MHD shock refraction problem. The solution technique is then outlined in § 3. Section 4 contains a detailed account of the quintuple-point solution for Samtaney's set of parameters, along with a comparison to his numerical results. A second solution that is not realized in the numerical simulation is also described. As B is decreased, we find that the types of waves arising from the shock refraction process undergo a number of transitions. These transitions in solution type are discussed in § 5. How the solutions approach the hydrodynamic triple-point in the limit of vanishing applied magnetic field is addressed in § 6. In § 7, the equations governing the leading-order asymptotic solution of the shock refraction problem in this limit are derived. The section concludes with a comparison between the asymptotic and full solutions. Finally, the conclusions that have emerged from this work are presented in § 8.

2. Formulation

2.1. *The governing equations of ideal MHD*

In this investigation, we will consider solutions to the equations of ideal MHD. These equations govern the motion of a quasi-neutral conducting fluid if viscosity, thermal conductivity, the Hall effect and electrical resistivity are neglected (Sutton & Sherman

https://doi.org/10.1017/S0022112004001880 Published online by Cambridge University Press

1965). The steady-state forms of these equations are

$$\nabla\cdot(\rho\boldsymbol{u}) = 0, \tag{2.1}$$

$$\rho(\boldsymbol{u}\cdot\nabla)\boldsymbol{u} = -\nabla p + \frac{1}{\mu_0}(\nabla\times\boldsymbol{B})\times\boldsymbol{B}, \tag{2.2}$$

$$\rho(\boldsymbol{u}\cdot\nabla)e_T = \frac{1}{\mu_0}(\nabla\times\boldsymbol{B})\times\boldsymbol{B}\cdot\boldsymbol{u}, \tag{2.3}$$

$$\nabla\cdot\boldsymbol{B} = 0, \tag{2.4}$$

$$\nabla\times(\boldsymbol{u}\times\boldsymbol{B}) = 0. \tag{2.5}$$

Here, ρ is the density, p is the pressure, $\boldsymbol{u}$ is the velocity, $\boldsymbol{B}$ is the magnetic field, μ_0 is the magnetic permeability, and $e_T = h + 1/2(\boldsymbol{u}\cdot\boldsymbol{u})$, where h is the enthalpy. In addition, the plasma is assumed to be a perfect gas with constant specific heats C_p and C_v. In this case

$$p = \rho RT,$$

$$h = C_pT,$$

$$e_T = \frac{\gamma}{\gamma-1}\frac{p}{\rho} + \tfrac{1}{2}\boldsymbol{u}\cdot\boldsymbol{u},$$

where T is temperature, $R = C_p - C_v$, and $\gamma = C_p/C_v$. In the sequel, we consider discontinuous solutions to these equations, solutions for expansion fans, solutions for compound waves and matching conditions at contact discontinuities. These are then combined to construct multiple-wave solutions corresponding to the interaction of a shock with an oblique density discontinuity.

2.2. *The MHD Rankine–Hugoniot relations*

The MHD Rankine–Hugoniot (RH) relations govern weak solutions to the equations of ideal MHD corresponding to discontinuous changes from one state to another. It is assumed that all dependent variables vary only in the direction normal to the shock front, which is denoted with the subscript n. Under this assumption, (2.4) implies that B_n is continuous across the shock. We also assume that all velocities and magnetic fields are coplanar, as we are seeking strongly planar ideal solutions. Under these assumptions, the set of jump relations for a stationary discontinuity separating two uniform states are (see e.g. Sutton & Sherman 1965),

$$[\rho u_n] = 0, \tag{2.6}$$

$$\left[\rho u_n^2 + p + \frac{B_t^2}{2\mu_0}\right] = 0, \tag{2.7}$$

$$\left[\rho u_n u_t - \frac{1}{\mu_0}B_nB_t\right] = 0, \tag{2.8}$$

$$\left[\frac{\rho u_n}{2}\left(u_n^2+u_t^2\right) + \frac{\gamma u_n p}{\gamma-1} + \frac{1}{\mu_0}u_nB_t^2 - \frac{1}{\mu_0}u_tB_nB_t\right] = 0, \tag{2.9}$$

$$[u_nB_t - u_tB_n] = 0. \tag{2.10}$$

Here, the subscript t denotes the component of a vector tangential to the shock, and $[A] \equiv A_2 - A_1$ denotes the difference in the quantity A between the states upstream (subscript 1) and downstream (subscript 2) of the shock.

We use the method of Kennel, Blandford & Coppi (1989) for obtaining solutions to the coplanar RH relations for propagating discontinuities ($u_{n1} \neq 0$). First, the

https://doi.org/10.1017/S0022112004001880 Published online by Cambridge University Press

following convenient set of normalized variables is introduced:

$$r = \frac{u_{n2}}{u_{n1}}, \quad b = \frac{B_{t2}}{B_1}, \quad U_t = \frac{u_{t2}}{u_{n1}}, \quad \sin\theta_1 = \frac{B_{t1}}{B_1},$$

where θ_1 is the angle between the upstream magnetic field and the shock normal. Also, reference upstream Alfvén, intermediate, and sonic Mach numbers are defined as

$$M_{A1}^2 = \frac{u_{n1}^2}{C_{A1}^2} = \frac{\mu_0\rho_1 u_{n1}^2}{B_1^2}, \quad M_{I1}^2 = \frac{u_{n1}^2}{C_{I1}^2} = \frac{M_{A1}^2}{\cos(\theta_1)^2} = \frac{\mu_0\rho_1 u_{n1}^2}{B_{n1}^2}, \quad M_{S1}^2 = \frac{u_{n1}^2}{C_{S1}^2} = \frac{\rho_1 u_{n1}^2}{\gamma p_1}.$$

It can then be shown that (2.6)–(2.9) reduce to the following algebraic equation in r and b obtained by Liberman & Velikhovich (1986):

$$F(r, b) = Ar^2 + B(b)r + C(b) = 0,$$

where A, B and C are defined in equations (A 2) and (A 3) in Appendix A. The relation $F(r, b) = 0$ defines a curve in (r, b) space on which the fluxes of mass, momentum and energy are equal to those upstream of the shock. The final jump condition can be expressed as

$$Z(r, b) = bX - Y\sin\theta_1 = 0,$$

where X and Y are defined in (A 3) and (A 5). The intersections of the curves defined by $F = 0$ and $Z = 0$ are the locations in (r, b) space where all jump conditions are satisfied. The two equations, $F = 0$ and $Z = 0$, can be combined into a quartic equation in r, which we know has at least one real solution ($r = 1$). Thus, the quartic must have either two or four real solutions, implying that there are either two or four intersections between the two curves. We refer to the three non-unity solutions of the quartic as roots A, B and C. Expressions for these roots are included in Appendix A. Figure 4 shows the curves $F = 0$ and $Z = 0$ for a choice of parameters where there are four intersections, labelled 1–4 in order of decreasing r. The velocities at each of these points bear a definite relationship to the fast (C_F), intermediate (C_I), and slow (C_{SL}) MHD characteristic speeds: $u_n(1) \geqslant C_F \geqslant C_I \geqslant C_{SL}$, $C_F \geqslant u_n(2) \geqslant C_I \geqslant C_{SL}$, $C_F \geqslant C_I \geqslant u_n(3) \geqslant C_{SL}$, and $C_F \geqslant C_I \geqslant C_{SL} \geqslant u_n(4)$. The entropies of the four states are ordered $S(1) \leqslant S(2) \leqslant S(3) \leqslant S(4)$, indicating that only six of the transitions between these states coincide with entropy-increasing shocks. Of these, transitions $1 \to 2$ are fast shocks, $3 \to 4$ are slow shocks, while $1 \to 3$, $1 \to 4$, $2 \to 3$, and $2 \to 4$ are intermediate shocks. Further details of how we solve the MHD RH relations for the flow state downstream of a shock are contained in Appendix A.

2.3. *Admissibility of MHD discontinuities*

To this point, we have discussed weak solutions to the ideal MHD equations. We now discuss their admissibility. This topic is an active research field and open questions remain. In the three-dimensional MHD system of equations, the evolutionary condition (see e.g. Akhiezer, Lubarski & Polovin 1959; Polovin & Demutskii 1990; Jeffrey & Taniuti 1964) restricts physically admissible discontinuities to fast shocks, slow shocks, contact discontinuities and rotational discontinuities (RDs). In a series of numerical experiments Wu (1987, 1990, 1995), however, identified intermediate shocks within numerical solutions to the full (here, full implies non-zero dissipation) MHD equations, which was interpreted as a failure of the evolutionary condition by Myong & Roe (1997) amongst others. Subsequently, Myong & Roe (1997) applied their viscosity

https://doi.org/10.1017/S0022112004001880 Published online by Cambridge University Press

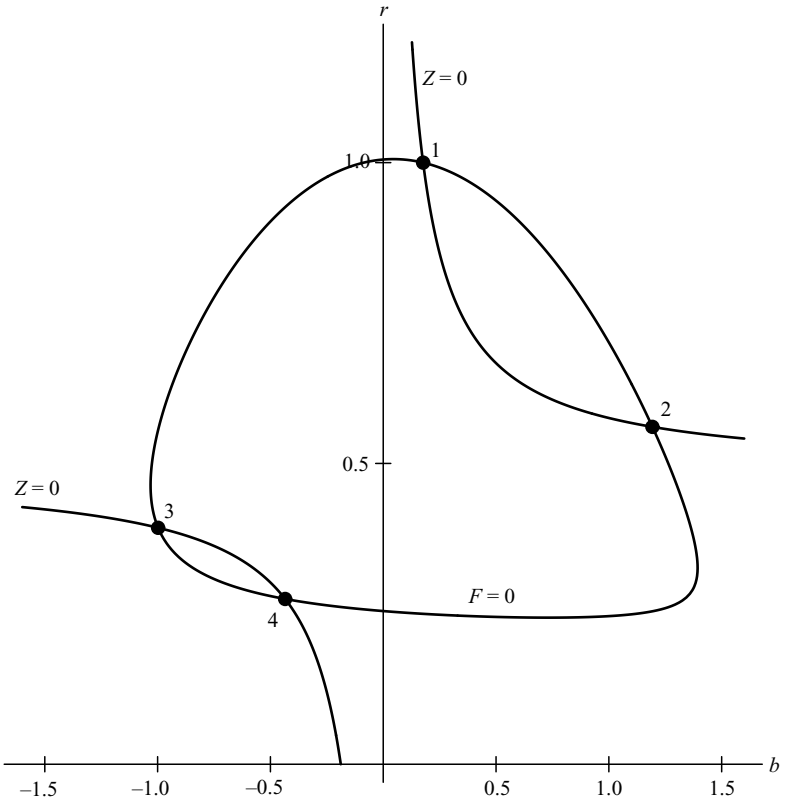


FIGURE 4. Graphical solution to the MHD Rankine–Hugoniot relations for $\sin^2\theta_1 = 1/32$, $M_{A1}^2 = 2$, $M_{S1} \to \infty$, and $\gamma = 5/3$ (choice of parameters from Kennel *et al.* 1989).

admissibility condition to show that in the strongly planar system $1 \to 3$, $1 \to 4$ and $2 \to 4$ intermediate shocks are physical, while $2 \to 3$ intermediate shocks are not. They also found that 180° RDs, which are a special case of $2 \to 3$ intermediate shocks, have no role in strongly planar problems. These results are in agreement with many numerical simulations by Wu (1987, 1990, 1995). In the full three-dimensional system, Wu (1990, 1995) observes $2 \to 3$ intermediate shocks to be possible, along with the other shock types, while RDs are regarded as unphysical. Wu (1990) also finds that the particular choice of dissipation coefficients can effect the admissibility of MHD shocks in the full system; see Wu (1990) and cited references therein for details.

Falle & Komissarov (2001) (hereinafter referred to as FK) argue that the viscosity admissibility condition and the evolutionary condition are complementary; a shock is physical only if it satisfies both. Hence, the subsets of discontinuities admissible in planar and strongly planar flows are not identical because only the former admit Alfvén waves. In this framework, $1 \to 3$ and $2 \to 4$ intermediate shocks along with slow (C_1) and fast (C_2) compound waves (using the notation in Myong & Roe 1997) are shown to be evolutionary (satisfy the evolutionary condition) and have unique dissipative structures in the strongly planar case. Both $2 \to 3$ intermediate shocks and 180° RDs are found to be non-evolutionary in the strongly planar system. These results are in agreement with those of Myong & Roe (1997). This is not the case for $1 \to 4$ intermediate shocks as these are shown to be non-evolutionary and hence

https://doi.org/10.1017/S0022112004001880 Published online by Cambridge University Press

inadmissible, although they do have a non-unique steady dissipative structure in the strongly planar case.

For the full three-dimensional MHD system, of which the planar (u_z, B_z may be non-zero) system is a subset, FK reiterate the following results: fast and slow shocks are evolutionary and have unique structurally stable dissipative structures, while all intermediate shocks are non-evolutionary and can be destroyed by interactions with Alfvén waves. Thus, in contrast to Wu (1987, 1990, 1995), FK argue that intermediate shocks are always inadmissible in the three-dimensional system. FK also state that, in the three-dimensional system, $1 \rightarrow 3$, $1 \rightarrow 4$ and $2 \rightarrow 4$ intermediate shocks possess non-unique steady dissipative structures, while $2 \rightarrow 3$ intermediate shocks possess a unique steady dissipative structure. CDs and RDs are found to be evolutionary but do not possess a steady dissipative structure as they are linear and hence have no nonlinear steepening to balance spreading due to dissipation. They nevertheless consider RDs to be admissible in the three-dimensional system, in contrast to Wu (1990, 1995). FK also analyse the admissibility of discontinuities that travel at the same speed as certain characteristics, such as switch-on and switch-off shocks.

To interpret our results, we have adopted the framework of FK because of its completeness, but we acknowledge that the physical relevance of intermediate shocks and RDs is not yet completely clarified. Following Torrilhon (2003*a*), we divide our solutions to the ideal MHD system into two categories: regular r and irregular c solutions. r-Solutions include only fast and slow waves (shocks or expansion fans), RDs and CDs. According to FK, all discontinuities in r-solutions are evolutionary in the planar system. Here, c-solutions are those that include discontinuities that are non-evolutionary in the planar system but are evolutionary in the strongly planar system according to FK.

2.4. *Governing equations for MHD expansion fans and slow compound waves*

The basic equations governing the flow through a centred steady MHD expansion fan can be obtained by writing (2.1)–(2.2) and (2.4)–(2.5) in cylindrical coordinates, then assuming variations only occur with the polar angle φ (Yang & Sonnerup 1976; Krisko & Hill 1991). Further, the flow is assumed to be isentropic; hence, the energy equation is replaced by an entropy equation. These equations can then be manipulated into a system of nonlinear coupled ODEs for a set of non-dimensional variables within the expansion fan. The system of ODEs and an outline of their derivation is contained in Appendix B. In the equations, the magnetic field is represented by the non-dimensional vector

$$\boldsymbol{K} \equiv \frac{\boldsymbol{B}}{\sqrt{2\mu_0 p}}.$$

Note that $K \equiv |\boldsymbol{K}| = \beta^{-1/2}$, $K_n = K\cos\theta$, and $K_t = K\sin\theta$, so $\boldsymbol{K}$ can be used interchangeably with (β, θ). Appendix B also includes the relation required to determine the location of the leading wavelet of an expansion fan. The complete solution throughout an expansion fan can be found by numerically integrating the system of ODEs with respect to φ from the leading wavelet.

In the strongly planar system, Myong & Roe (1997) recommend the use of compound waves as a substitute for $2 \rightarrow 3$ intermediate shocks, which are inadmissible under their viscosity admissibility condition and the evolutionary condition. Compound waves are discussed in more detail in Appendix C. The compound wave relevant to this study consists of a $2 \rightarrow 3 = 4$ intermediate shock, for which $u_{n2} = C_{SL2}$, followed immediately downstream by a slow-mode expansion fan. This is the steady two-dimensional analogue of the unsteady one-dimensional slow compound wave

https://doi.org/10.1017/S0022112004001880 Published online by Cambridge University Press

referred to as C_1 by Myong & Roe (1997). We will use the same designation for the two-dimensional compound wave. A relation for determining the location of a $2 \rightarrow 3 = 4$ intermediate shock is included in Appendix C, along with a procedure for determining the flow state downstream of a C_1 compound wave.

2.5. *Matching conditions at the contact discontinuity*

For the proposed wave configuration to be a valid solution of the equations of ideal MHD, the following matching conditions must hold across the shocked contact (SC):

$$p_3 = p_5, \tag{2.11}$$

$$u_{3x} = u_{5x}, \tag{2.12}$$

$$u_{3y} = u_{5y}, \tag{2.13}$$

$$|\boldsymbol{K}_3| = |\boldsymbol{K}_5|, \tag{2.14}$$

$$\boldsymbol{K}_3/|\boldsymbol{K}_3| = \boldsymbol{K}_5/|\boldsymbol{K}_5|. \tag{2.15}$$

Here, states 3 and 5 are the conditions to the left and right of the SC, respectively. This is indicated in figure 5, which shows how the various angles and regions of uniform flow in a solution are defined. In Appendix D, we outline our procedure for determining the conditions on either side of the SC from the problem parameters and guessed values of the unknown wave angles.

3. Solution technique

We seek solutions to the strongly planar ideal MHD equations. In the equivalent dissipative solutions, the out-of-plane components of $\boldsymbol{B}$ and $\boldsymbol{u}$ may be non-zero within the internal structures of certain waves. This implies that some of our solutions are planar, not strongly planar, in the presence of dissipation. For a given set of problem parameters, $(M, \beta, \eta, \alpha, \gamma)$, a solution to the MHD shock refraction problem is obtained by first postulating a wave configuration. We restrict our attention to wave configurations in which the number of unknown wave angles equals the number of independent matching conditions at the SC (four). Families of solutions may be possible if additional waves are introduced, for example, by replacing a $2 \rightarrow 4$ intermediate shock or a C_1 compound wave by a $2 \rightarrow 3$ intermediate shock followed by a slow wave (shock or expansion fan). Wu (1995) found this for certain coplanar MHD Riemann problems, which are analogous to the flows considered here. We remark that the families of solutions identified by Wu (1995) appear to always include $2 \rightarrow 3$ intermediate shocks; we have not considered structures involving this shock type in depth as they are inadmissible according to FK. For the range of parameters under consideration here, for which *RF* and *TF* are always fast shocks, a wave configuration is postulated by specifying whether the *RS* and/or the *TS* wave group consists of a shock, a C_1 compound wave, an RD, an RD followed by a slow shock, or an RD followed by a slow-mode expansion fan. Next, the types of all shocks in the system must be specified by selecting which root of (A 6) is used to compute r for each shock. Once the wave configuration has been specified in this manner, guesses are made for each of the four unknown angles in the system: ϕ_1, ϕ_2, ϕ_3 and ϕ_4. As indicated in figure 5, ϕ_1 specifies the location of shock *RF*, ϕ_2 specifies either the location of shock *RS* or the last expansion fan wavelet in wave group *RS*, ϕ_3 specifies the location of shock *TF*, and finally, ϕ_4 specifies either the location of shock *TS* or the last expansion fan wavelet in wave group *TS*, depending on the wave configuration postulated. The procedure outlined in Appendix D is then

https://doi.org/10.1017/S0022112004001880 Published online by Cambridge University Press

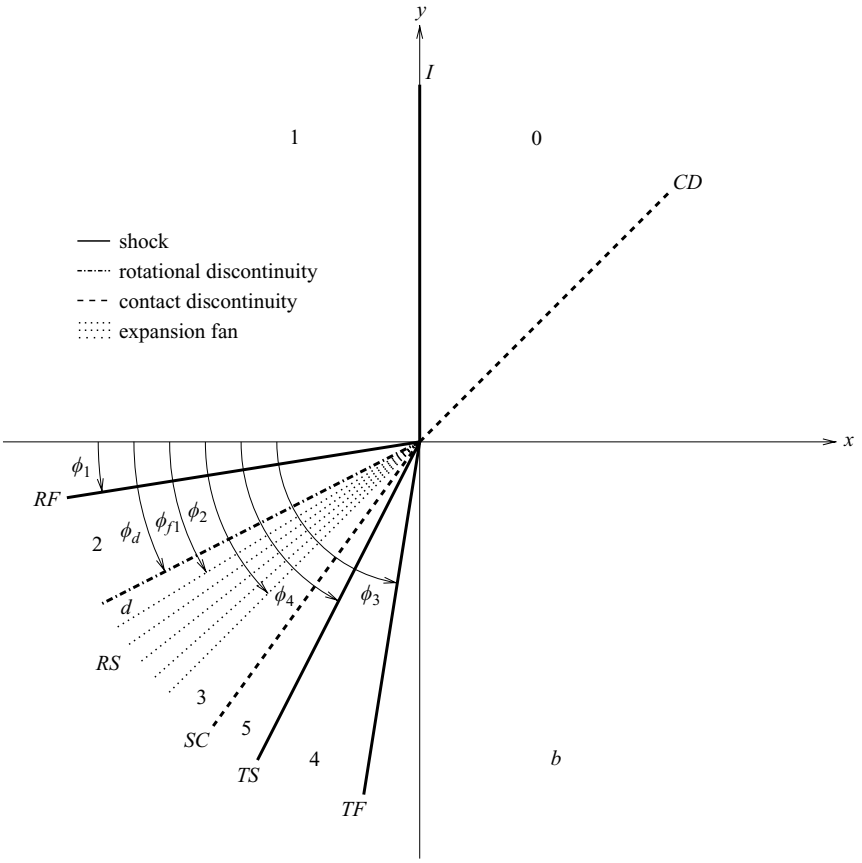


FIGURE 5. Designations of the angles and regions of uniform flow for a shock refraction problem where the *RS* wave group consists of an RD followed by a slow-mode expansion fan, and the *TS* wave is a shock. This type of solution is referred to as a *sextuple-point*. The undisturbed conditions to the left and right of the CD are denoted states 0 and *b*, respectively.

used to compute the conditions on either side of the SC for the guessed wave angles. An approximate solution to the MHD shock refraction problem is then obtained by iterating on the wave angles using a secant method until matching conditions (2.11)–(2.14) are satisfied to six significant figures. To check the consistency of this procedure, the wave angles obtained from the iterative process are then substituted into matching condition (2.15) to ensure that it is also satisfied.

4. A detailed local solution; Case S1

In subsequent sections, we will explore several branches corresponding to the solution of (2.11)–(2.14) in the parameter space of M, η, α, β and γ. For the purposes of discussion, we define a branch to be a set of solutions along a line in parameter space that all satisfy the same admissibility condition. The lines in parameter space considered here have fixed M, η, α and γ with β in the range $\beta_{min} \leqslant \beta \leqslant \beta_{max}$. We will study in detail solutions along four such lines that we denote as Lines I–IV. The parameters defining these are summarized in table 1. To illustrate the application of our solution technique for a particular case, we choose Line I ($M = 2, \eta = 3, \alpha = \pi/4$,

https://doi.org/10.1017/S0022112004001880 Published online by Cambridge University Press

Line	I	II	III	IV
M	2	2	2	1.4
α	$\pi/4$	$\pi/4$	$\pi/4$	$\pi/4$
η	3	3	1.5	3
γ	1.4	5/3	5/3	5/3
β_{min}	2	2	2	2
$\beta_{max}^{(c)}$	61.6	9.28	34.0	49.5
$\beta_{max}^{(r)}$	2.39×10^7	102 968	104 385	103 339

TABLE 1. Parameters defining Lines I–IV. $\beta_{max}^{(c)}$ and $\beta_{max}^{(r)}$ are the maximum values of β for the c- and r-branches associated with each line.

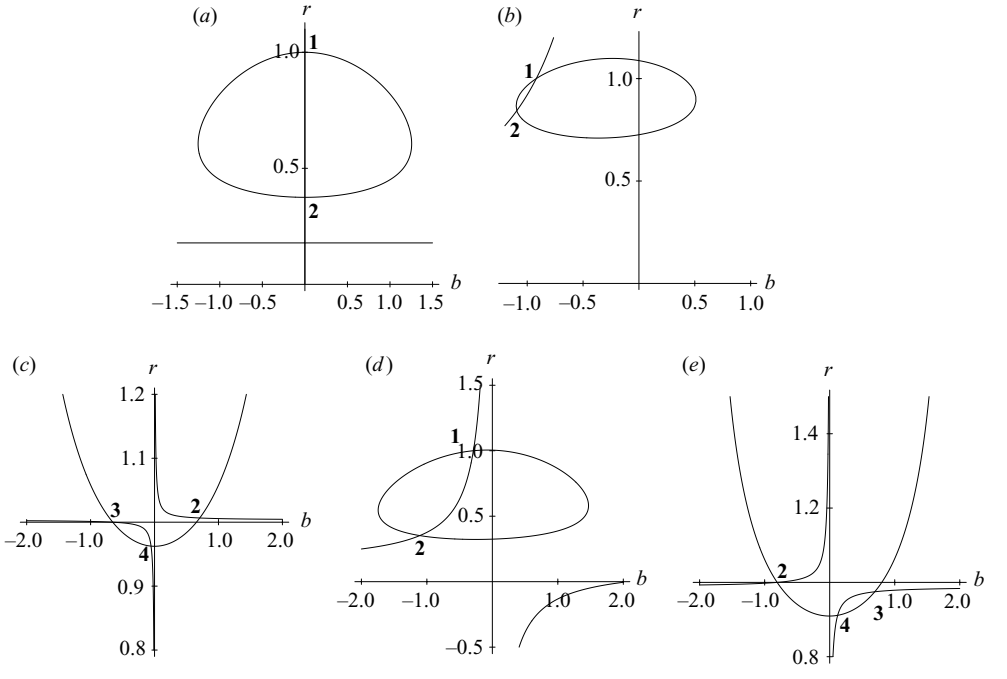


FIGURE 6. Graphical solutions of the MHD Rankine–Hugoniot relations for conditions upstream of (*a*) shock *I*, (*b*) shock *RF*, (*c*) shock *RS*, (*d*) shock *TF*, (*e*) shock *TS* in case S1.

and $\gamma = 1.4$) with $\beta = \beta_{min} = 2$. This parameter set corresponds to that used by Samtaney (2003). In the following discussion, for convenience, we denote this as case S1.

4.1. *Irregular solution*

First, we examine the solution suggested by Samtaney's numerical results, in which four shocks arise from the shock refraction process for case S1. We demonstrate that this is a *c*-solution. Including the incident shock, there are five shocks in the system, hence the solution is referred to as a quintuple-point. The incident shock is hydrodynamic and has no effect on the magnetic field, as can be seen from figure 6(*a*), which shows the graphical solution of the RH relations for the conditions upstream of this shock. The value of r for this shock is given by root A of the RH relations.

https://doi.org/10.1017/S0022112004001880 Published online by Cambridge University Press

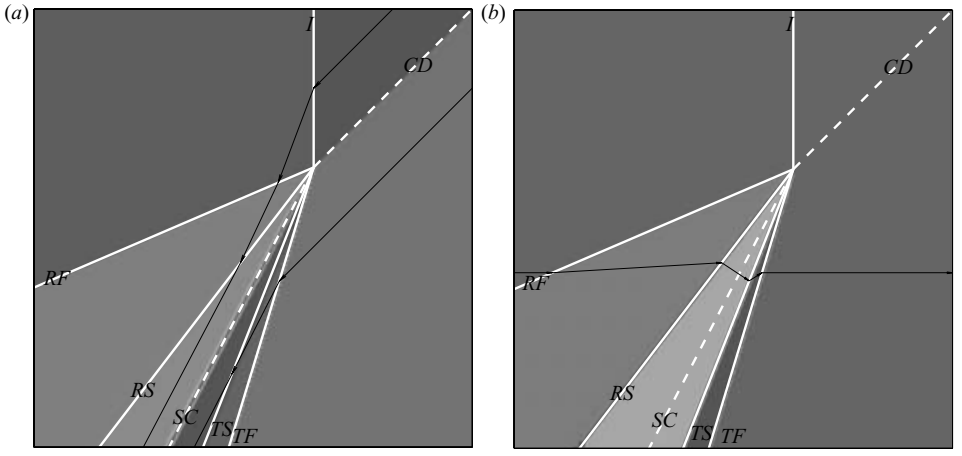


FIGURE 7. Computed shock and CD angles for case S1 (c-solution) overlaid on (a) density contours and (b) B_y contours from the numerical results of Samtaney (2003). Sample streamlines and field lines are shown in (a) and (b), respectively.

In this instance root A is the only real root, disregarding $r = 1$, and gives $r_0 = 0.375$ while $b_0 = 0$. Note that hydrodynamic shocks are non-evolutionary if the upstream u_n is super-Alfvénic and the downstream u_n is sub-Alfvénic in the reference frame of the shock. This criteria is not met for case S1 so the incident shock is evolutionary, as is the case for all other sets of parameters considered here. With reference to figure 5, *RF* was found to lie at $\phi_1 = 0.405693$ and is a fast shock. Root A gives $r_1 = 0.844$ resulting in $b_1 = -1.09$. Figure 6(b) shows that this is the only real root other than 1. *RS* is a slow shock and was found to lie at $\phi_2 = 0.917018$. Figure 6(c) shows that all three roots are real for *RS*, but as intersection 3 corresponds to the upstream state, only a transition to intersection 4 will result in $r_2 < 1$ and thus satisfy the entropy condition. This transition corresponds to a slow shock for which root B gives the value of r. r_2 and b_2 were found to be 0.963 and -0.0547, respectively. *TF* was found to lie at $\phi_3 = 1.27673$ and is a fast shock for which root A gives $r_b = 0.352$, while $b_b = -1.11$. Finally, *TS* is a $2 \rightarrow 4$ intermediate shock and was found to lie at $\phi_4 = 1.19426$. The presence of this intermediate shock implies that this quintuple-point is a c-solution, which we denote solution S1c. Figure 6(e) shows that all three roots are real for *TS* and intersection 2 corresponds to the upstream state. A transition to intersection 1, corresponding to root A, would violate the entropy condition. A transition to intersection 3, corresponding to root C, satisfies the entropy condition but it was found that, for case S1, the matching conditions (2.11)–(2.15) could not be satisfied if *TS* was assumed to be a $2 \rightarrow 3$ intermediate shock. Thus, r_4 is given by root B and was found to be 0.911 while $b_4 = 0.122$.

The shock and CD angles from solution S1c are overlaid on the numerical results of Samtaney (2003) in figure 7. Figure 7(a) shows contours of density which clearly display the location of the CD. Streamlines are also plotted in this figure to show how the various shocks in the system deflect the flow. In region 2, the streamlines are angled toward the SC. Shock *RS* then deflects them away from the shock normal, aligning them with the SC in region 3. Conversely, in region 4, the streamlines are angled away from the SC and shock *TS* brings them into alignment by deflecting them toward the shock normal. This type of deflection is not possible for hydrodynamic shocks as they do not support a tangential velocity jump. Figure 7(b) shows contours

https://doi.org/10.1017/S0022112004001880 Published online by Cambridge University Press

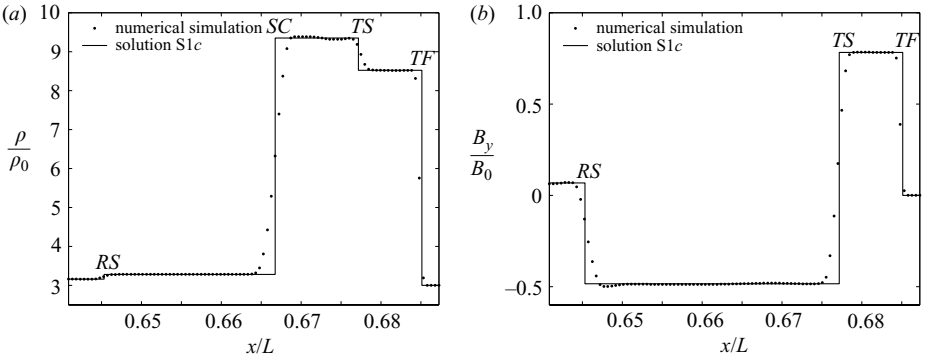


FIGURE 8. Normalized profiles of (*a*) ρ and (*b*) B_y from the numerical results of Samtaney (2003) at $y/L = 0.62524$ compared to profiles from solution S1*c*. L is the vertical extent of the computational domain. *RF* is not shown because it is in a coarse region of the computational grid and is at a shallow angle to the x-axis, hence its structure is highly diffuse. The profiles have been aligned such that the centre of the SC lies at the same location in each profile. They could not be aligned exactly owing to the uncertainty in the location of the intersection point in the numerical results.

of B_y to clearly display the locations of the weaker shocks that have small density jumps across them. A typical magnetic field line is also plotted in this figure to show how the various shocks in the system deflect the field. Figure 8 shows normalized ρ and B_y profiles along a horizontal line that passes though *RS*, the SC, *TS* and *TF*. Profiles from solution S1*c* are compared to those from the numerical results of Samtaney (2003). From figures 7 and 8, it can be seen that there appears to be close agreement between solution S1*c* and the numerical results.

4.2. *Regular solution*

In general, ideal *c*-solutions are not unique because a corresponding *r*-solution exists (see e.g. Torrilhon 2003*b*). This is so for solution S1*c*. The corresponding *r*-solution, which we denote solution S1*r*, has the same structure except that the *TS* wave group consists of an RD followed downstream by a slow shock. As this structure involves six shocks/RDs, it is referred to as a sextuple-point solution. The combined properties of the transmitted RD and slow shock are similar to those of the $2 \rightarrow 4$ intermediate shock in the *c*-solution; the sign of B_t is reversed and the flow is compressed. This allows the locations of the other shocks in the *r*-solution to remain relatively unchanged from solution S1*c*, as can be seen from examination of the shock angles. For solution S1*r*, these were found to be $\phi_1 = 0.405694$, $\phi_2 = 0.917019$, $\phi_3 = 1.27678$ and $\phi_4 = 1.19283$. With the exception of the angle of the transmitted slow shock, ϕ_4, these angles differ from those in solution S1*c* only in the sixth significant figure.

5. Transitions in solution type with decreasing magnetic field magnitude

We will now examine how solutions to the shock refraction problem vary with certain parameters. Our main focus will be on how the solutions change as β is increased. To study this, we have computed solutions along four lines in parameter space, which are defined in table 1. Regular and irregular solution branches exist for each line. We begin our examination by identifying transitions in solution type that occur along the irregular branch associated with Line I (Branch I*c*), for which solution S1*c* is the minimum β solution. The examination is repeated for the regular branch

https://doi.org/10.1017/S0022112004001880 Published online by Cambridge University Press

associated with Line I (Branch Ir). We then examine a number of mathematical solutions to the shock refraction problem that are non-evolutionary in both the planar and strongly planar MHD systems, according to FK. The branches associated with Lines II–IV indicate how the transition points vary for certain changes in M, η and γ. In § 6, we extend this investigation to the limit of large β and examine how the limiting solutions are related to the hydrodynamic triple-point, which occurs for $\beta^{-1} = 0$.

5.1. *Branch Ic*

We begin to follow Branch Ic by computing a solution for a value of β that is 0.001% greater than β_{min}, using the shock angles from solution S1c as the initial guesses in the iterative solution procedure. Two more solutions along the branch are then computed by successively incrementing β by 0.001% and using the previously computed shock angles as the initial guesses. Once these first four solutions have been obtained, the initial guesses for the shock angles are computed using third-order extrapolation in β. This allows β to be increased by larger increments of 2% to 5% while still providing sufficiently accurate initial guesses for the iterative solution procedure to converge rapidly.

For the initial part of the solution branch beginning at $\beta_{min} = 2$, figure 9(a) shows how the angles of fast shocks RF and TF deviate from their corresponding triple-point values; the angles of shocks R and T in hydrodynamic triple-point solution to the shock refraction problem with $M = 2$, $\eta = 3$, $\alpha = \pi/4$, $\gamma = 1.4$ and $\beta^{-1} = 0$. This reveals that as β is increased, the fast shock angles tend toward their triple-point values. As this occurs, the misalignment between the flow in region 2 and that in region 4 decreases. Thus, the magnitudes of the angles through which shocks RS and TS must deflect the flow (δ_2 and δ_4, respectively) decrease, as can be seen from figure 9(b). Figure 9(c) shows how the values of roots B and C vary for the conditions upstream of shock RS. At the beginning of Branch Ic, r_2 is given by root B, corresponding to a slow shock. As β is increased, the required decrease in the magnitude of δ_2 is achieved by the shock becoming weaker, as indicated by the value of r_2 increasing toward unity. At $\beta \approx 2.32$, the value of root C drops to 1 and RS is a switch-off shock. Beyond this, the value of root C drops below 1 so that the state upstream of RS now corresponds to intersection 2 of the $F = 0$ and $Z = 0$ curves. This implies that RS has transitioned from a slow shock to a $2 \rightarrow 4$ intermediate shock, as can be seen from figures 10(a) and 10(b), which show the graphical solution to the RH relations for shock RS for values of β bracketing the transition point. We denote this a Slow-I24 transition.

Figure 9(c) shows that as β is increased further, roots B and C converge and become equal at $\beta \approx 4.68$, where RS is a $2 \rightarrow 3 = 4$ intermediate shock. At this value of β, the lower branch of the $Z = 0$ curve is tangent to the $F = 0$ curve, as shown in figure 10(c). For the solution branch to continue beyond this point, shock RS must continue to weaken as β increases. This may be achieved by RS transitioning from a $2 \rightarrow 4$ to a $2 \rightarrow 3$ intermediate shock, for which r_2 is given by root C instead of root B. We denote this a I24-I23 transition. Figure 9(c) shows that this transition allows r_2 to continue to increase smoothly for $\beta > 4.68$. According to FK, the $2 \rightarrow 3$ intermediate shock present in the solutions beyond the I24-I23 transition is non-evolutionary in both the planar and strongly planar MHD systems. For this reason, we do not consider these solutions as belonging to Branch Ic. Alternatively, Branch Ic may be continued via a slow-mode expansion fan appearing immediately downstream of the $2 \rightarrow 3 = 4$ intermediate shock, forming a C_1 compound wave that is evolutionary in

https://doi.org/10.1017/S0022112004001880 Published online by Cambridge University Press

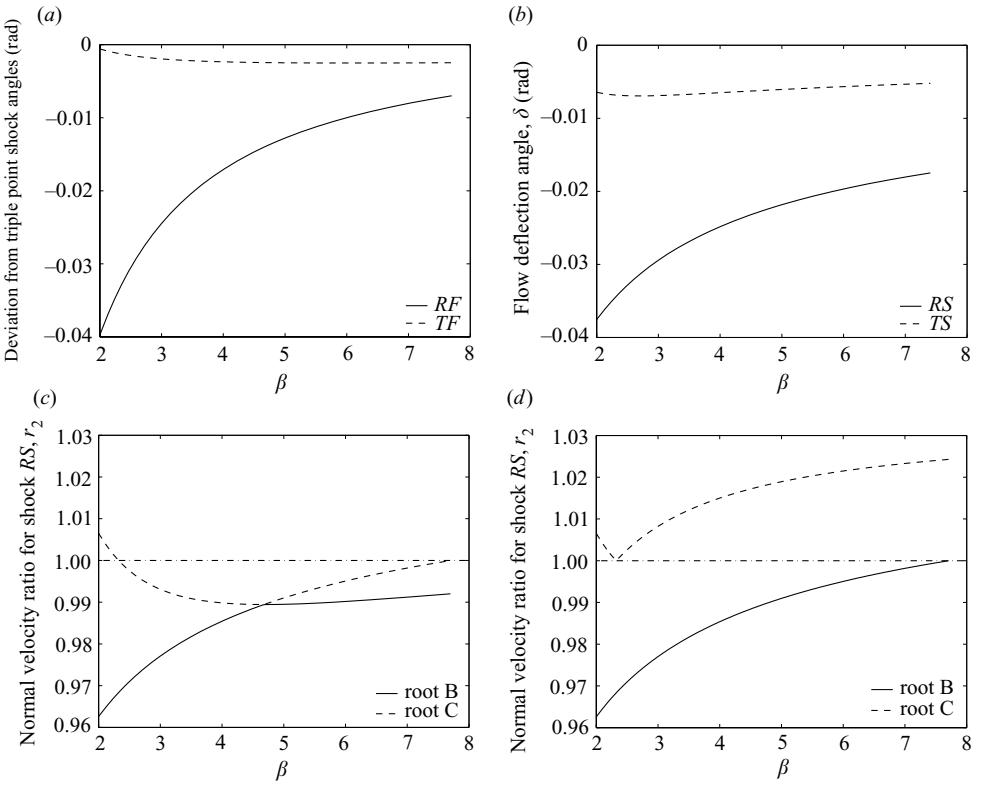


FIGURE 9. (*a*) Deviation of the fast shock angles from their corresponding values in the hydrodynamic triple-point, (*b*) angular deflection of the flow through *RS* and *TS*, and (*c*) roots B and C for the conditions upstream of *RS* for the initial part of solution Branch I*c* (values of roots B and C for $\beta > 4.68$ are not associated with Branch I*c*) with $M = 2$, $\eta = 3$, $\alpha = \pi/4$ and $\gamma = 1.4$. (*d*) Roots B and C for the conditions upstream of the slow shock in the *RS* wave group for the initial part of solution Branch I*r*.

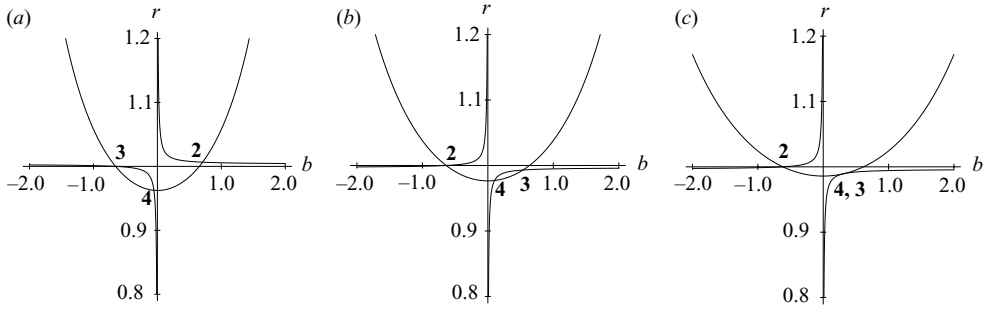


FIGURE 10. Graphical solutions of the MHD Rankine–Hugoniot relations for conditions upstream of shock *RS* along Branch I*c* at (*a*) $\beta = 2$, (*b*) $\beta = 3$ and (*c*) $\beta = 4.68$.

the strongly planar system according to FK. We denote this a I24-C_1 transition. It was found that RS does not undergo any further transitions with increasing β after the I24-C_1 transition occurs. For Branch I*c*, *TS* undergoes the Slow-I24 transition at $\beta \approx 0.964$, which is beyond where we have defined the end of Line I. For values of β

https://doi.org/10.1017/S0022112004001880 Published online by Cambridge University Press

Shock	Transition pair	Line I	Line II	Line III	Line IV
RS	Slow-RdSlow/Slow-I24	2.32	2.48	10.2	13.8
	I24-C_1/I24-I23	4.68	4.96	20.5	28.2
	RdSlow-RdExp/I23-RdExp	7.71	8.17	34.0	47.3
TS	Slow-RdSlow/Slow-I24	0.964	1.11	5.12	9.13
	I24-C_1/I24-I23	4.79	4.50	16.3	25.2
	RdSlow-RdExp/I23-RdExp	10.2	9.28	32.6	48.5

TABLE 2. Values of β where transitions in solution type occur for Lines I–IV. The values of β given are accurate to the displayed number of significant figures. Pairs of transitions, such as the I24-C_1 and I24-I23 transitions, occur at the same β value up to the accuracy displayed here. Not all pairs of transitions necessarily coincide.

just below this transition point, the c- and r-solutions are identical, but the solution branch terminates at $\beta \approx 0.952$ where the incident shock becomes non-evolutionary. *TS* was found to undergo the I24-C_1 transition at a slightly higher value of β than *RS*. All identified transition points are specified in table 2.

5.2. *Branch Ir*

Solution S1r is the starting point for Branch Ir. As for Branch Ic, both *RS* and *TS* weaken (r and $|\delta|$ decrease) as β is increased along Branch Ir. *RS* is initially a slow shock with r_2 given by root B. It weakens to a switch-off shock at $\beta \approx 2.32$, where root C is equal to 1. This can be seen from figure 9(d), which shows roots B and C for the conditions upstream of the slow shock in the *RS* wave group along the initial portion of Branch Ir. Rather than undergoing a Slow-I24 transition at this point, an RD appears upstream of the shock. This event allows the sign of B_t to be reversed across the *RS* wave group without the trailing shock becoming intermediate and is denoted a Slow-RdSlow transition. Figure 9(d) shows that root C increases above unity after the Slow-RdSlow transition, confirming that the trailing shock remains slow. As β is increased beyond this transition point, the trailing slow shock continues to weaken. It becomes a slow magneto-acoustic wave that has no effect on the flow at $\beta \approx 7.71$, where r_2 reaches unity. In order for Branch Ir to continue for $\beta > 7.71$, the magnitude of δ_2 must be decreased further. This is achieved by the slow magneto-acoustic wave transitioning to a slow-mode expansion fan. We denote this process a RdSlow-RdExp transition. It was found that the *RS* wave group does not undergo any further transitions with increasing β. The *TS* wave group also undergoes the Slow-RdSlow and RdSlow-RdExp transitions, the locations of which are specified in table 2.

Each possible combination of *RS* and *TS* wave groups is referred to as a solution type. The ranges of β for which each solution type is valid are shown in figure 11 for Branches Ic and Ir, along with the angular width of the inner layer. The angular width of the inner layer is defined as the angle from the leading wave in the *RS* wave group to the leading wave in the *TS* wave group. Also shown in figure 11 are values of β for which we compare our results to the numerical simulations of Samtaney (2003) and present simulations of the same type.

5.3. *Non-evolutionary solutions on Line I*

For completeness, we will now briefly examine a number of mathematical solutions to the shock refraction problem that are non-evolutionary in both the planar and

https://doi.org/10.1017/S0022112004001880 Published online by Cambridge University Press

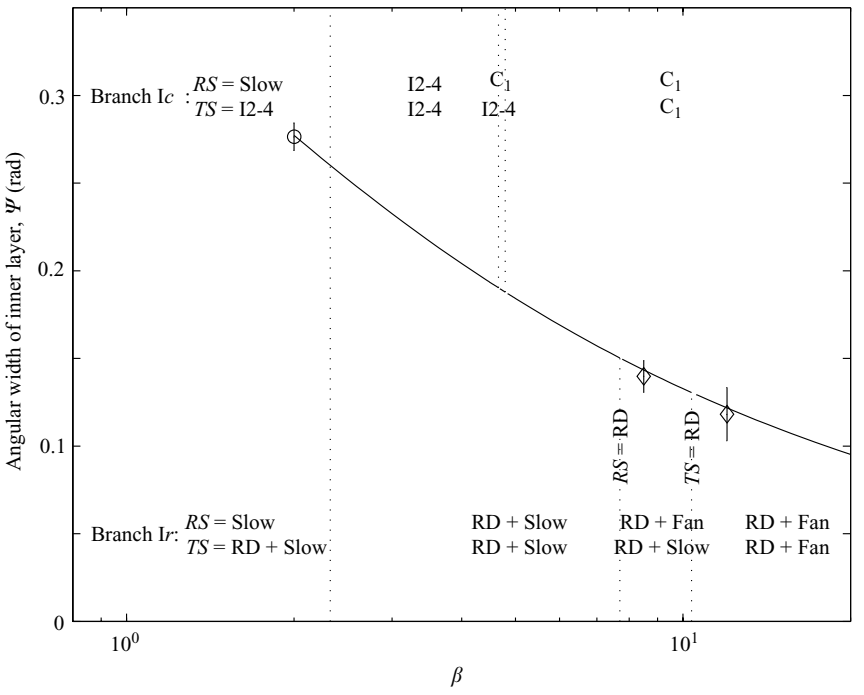


FIGURE 11. Locations of transitions in solution type with increasing β along Branches Ic and Ir ($M = 2$, $\eta = 3$, $\alpha = \pi/4$, $\gamma = 1.4$). The angular width of the inner layer (Ψ) from Branch Ic is indistinguishable from that from Branch Ir on the scale of this plot. I2-4 designates a $2 \rightarrow 4$ intermediate shock. ○, inner-layer widths from the numerical simulations of Samtaney (2003). ◇, inner-layer widths from present numerical simulations. The error bars correspond to 95% confidence intervals for the inner-layer widths computed from the numerical simulations.

strongly planar MHD systems according to FK. Perhaps the most significant of these solutions are those involving $2 \rightarrow 3$ intermediate shocks. Such solutions can arise from RS and TS undergoing the I24-I23 transition identified in § 5.1. As discussed in § 3, other solutions involving $2 \rightarrow 3$ intermediate shocks may exist, but we have not investigated this. Computing the solutions in which RS and TS undergo the I24-I23 transition for increasing β along Line I, we find that r_2 reaches unity at $\beta \approx 7.71$, as can be seen from figure 9(c). At this value of β, the reflected $2 \rightarrow 3$ intermediate shock has weakened to the point where it has become an RD. For the non-evolutionary sub-branch (set of solutions valid along a portion of Line I) to continue for $\beta > 7.71$, the magnitude of δ_2 must decrease further. This can be achieved computationally via an expansion shock, for which $r > 1$. Expansion shocks, however, are entropy decreasing and thus non-physical. Alternatively, a slow-mode expansion fan may be introduced downstream of the RD to turn the flow toward the SC and bring it into alignment with that in region 5. We denote this a I23-RdExp transition. After both RS and TS undergo the I23-RdExp transition, the solutions lie on Branch Ir and are evolutionary in the planar system according to FK. Figure 12 illustrates the relationships between the various branches associated with Line I. It shows the angle between the leading wave in the RS wave group and the location where a reflected RD would occur in solutions along Line I. This angle is zero when the RS wave group contains an RD. Note that the transitions of TS must also be considered to gain a complete understanding of the branch structure.

https://doi.org/10.1017/S0022112004001880 Published online by Cambridge University Press

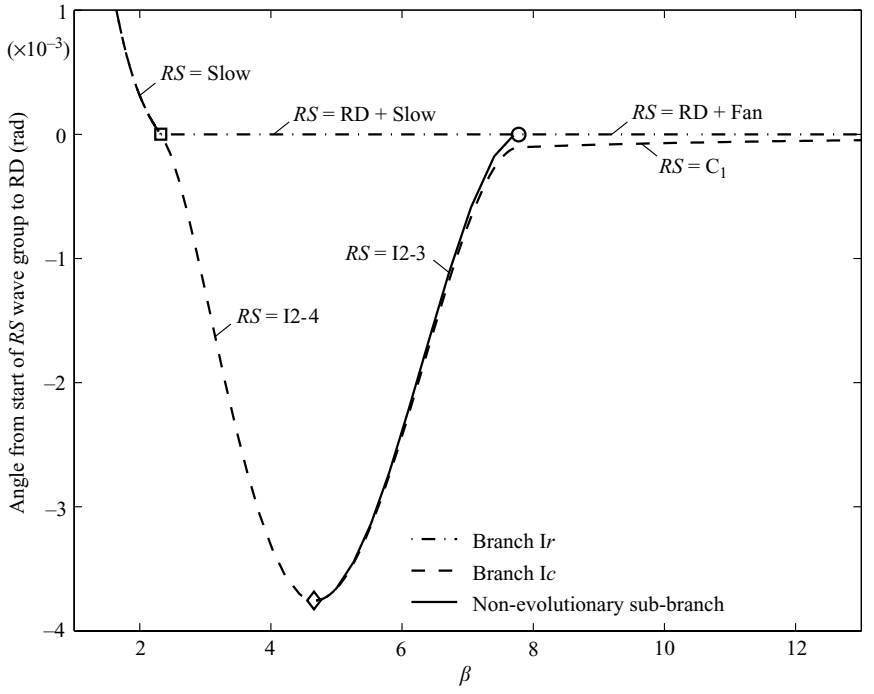


FIGURE 12. Angular separation between the leading wave in the RS wave group and the location where a reflected RD would appear in solutions along the various branches associated with Line I. Note that, in many solutions, the RD is non-existent. □, the Slow-RdSlow/Slow-I24 transition point. ◇, the I24-C_1/I24-I23 transition point. ○, the RdSlow-RdExp/I23-RdExp transition point. Note also that the pairs of transition points (e.g. the Slow-RdSlow and Slow-I24 transition points) may not coincide exactly, although they appear to do so on the scale of this plot. I2-3 and I2-4 designate $2 \rightarrow 3$ and $2 \rightarrow 4$ intermediate shocks, respectively.

It is possible to find solutions that satisfy (2.11)–(2.15) where the *RS* and *TS* wave groups consist of an RD followed by an expansion fan for values of β below their RdSlow-RdExp transition points. These solutions require the final expansion fan wavelets to be positioned upstream of the leading wavelets, hence they are non-physical.

Additional non-evolutionary solutions are possible if *RS* and *TS* undergo different transitions. For example, if *RS* undergoes Slow-RdSlow and RdSlow-RdExp transitions while *TS* undergoes Slow-I24 and I24-C_1 transitions, or vice versa. After *RS* and *TS* have each undergone at least one transition, these solutions are not evolutionary in either the planar or strongly planar systems, hence we have not studied them in detail.

5.4. *Lines II–IV*

We will now investigate whether the same set of transitions occurs along Lines II–IV, which are defined in table 1. The minimum β endpoints of these branches are denoted as cases S2, S3 and S4, respectively. The parameters for case S2 are the same as those for case S1 with the exception of γ, which is increased to 5/3, a value more typically associated with plasma. The *c*- and *r*-solutions to case S2 were found by following the solution branches corresponding to increasing γ from the case S1 solutions. No transitions in solution type occur along these branches. For case S3, η is set to 1.5 to investigate the effects of reducing the density ratio. The other parameters are identical

https://doi.org/10.1017/S0022112004001880 Published online by Cambridge University Press

to those for case S2. Along the regular and irregular solution branches between the case S2 and case S3 solutions, the *RS* wave group undergoes I24-Slow and RdSlow-Slow transitions, respectively. For case S4, M is set to 1.4 to investigate the effects of reducing the Mach number. The other parameters are identical to those for case S2. Along the regular and irregular solution branches between the case S2 and case S4 solutions, the *RS* wave group undergoes I24-Slow and RdSlow-Slow transitions, respectively.

The branches associated with Lines II–IV emanate from the solutions to cases S2-S4, respectively, and are computed for increasing β in the same manner as Branch I*c*. The sets of transitions in solution type that occur along Lines II–IV were found to be the same as those along Line I, but the order in which the transitions occur was found to vary. Along Lines II and IV, *TS* undergoes the I24-C_1/I24-I23 transition before *RS*, but *RS* is the first to undergo the RdSlow-RdExp/I23-RdExp transition. Along Line III, *TS* undergoes all transitions at lower values of β than *RS*. The values of β at which the transitions occur along all solution branches investigated are given in table 2. Note that while the pairs of transitions, such as the I24-C_1 and I24-I23 transitions, occur at the same β value up to the accuracy displayed in the table, not all pairs of transitions necessarily coincide exactly. From this table, we see that the increase in γ from Line I to Line II causes all transitions of *TS* except for the Slow-RdSlow to occur earlier, while it delays the transitions of *RS*. Both the decrease in M from Line II to Line III and the decrease in η from Line II to Line IV cause all transitions to occur at significantly larger β values.

6. Approach to the hydrodynamic triple-point: a singular limit

At values of β higher than the transition points given in table 2, we have identified two flow structures that may be produced by the shock refraction process for each of the four parameter sets considered here. These two structures are the *septuple-point r*-solution, which consists of a combination of seven shocks, RDs, and expansion fans, and a *quintuple-point c*-solution consisting of a combination of five shocks and compound waves. The behaviour of these solutions at large β is the topic of the following subsections. We present the behaviour of the septuple-point first because it is more geometrically complex and efficient to compute for reasons that will be discussed in § 6.2.

6.1. *Behaviour of septuple-point solutions at large* β

The structure of the septuple-point *r*-solution is illustrated in figure 13(*a*). In the septuple-point solution, *RF* and *TF* are fast shocks, the *RS* wave group consists of an RD, labelled *RRD*, followed downstream by a slow-mode expansion fan, labelled *RFan*, and finally, the *TS* wave group consists of an RD, labelled *TRD*, followed downstream by a slow-mode expansion fan, labelled *TFan*. Following Branch I*r* revealed that the septuple-point flow structure is maintained for β values up to 2.39×10^7. Solutions for β values greater than this were not computed.

Figure 13(*b*) reveals that as the magnetic field weakens, the angular width of the inner layer Ψ diminishes, while figure 13(*c*) shows that the shock locations converge to their corresponding triple-point values for large β. The slope of the Ψ versus β^{-1} curve, when plotted on a logarithmic scale, reveals that Ψ scales as $\beta^{-1/2}$, which is proportional to the applied magnetic field magnitude B. Figure 13(*d*) shows the jump in velocity tangential to the SC across the inner layer, $\Delta u_{t\,inner}$, normalized by the jump in tangential velocity across the SC in the corresponding triple-point

https://doi.org/10.1017/S0022112004001880 Published online by Cambridge University Press

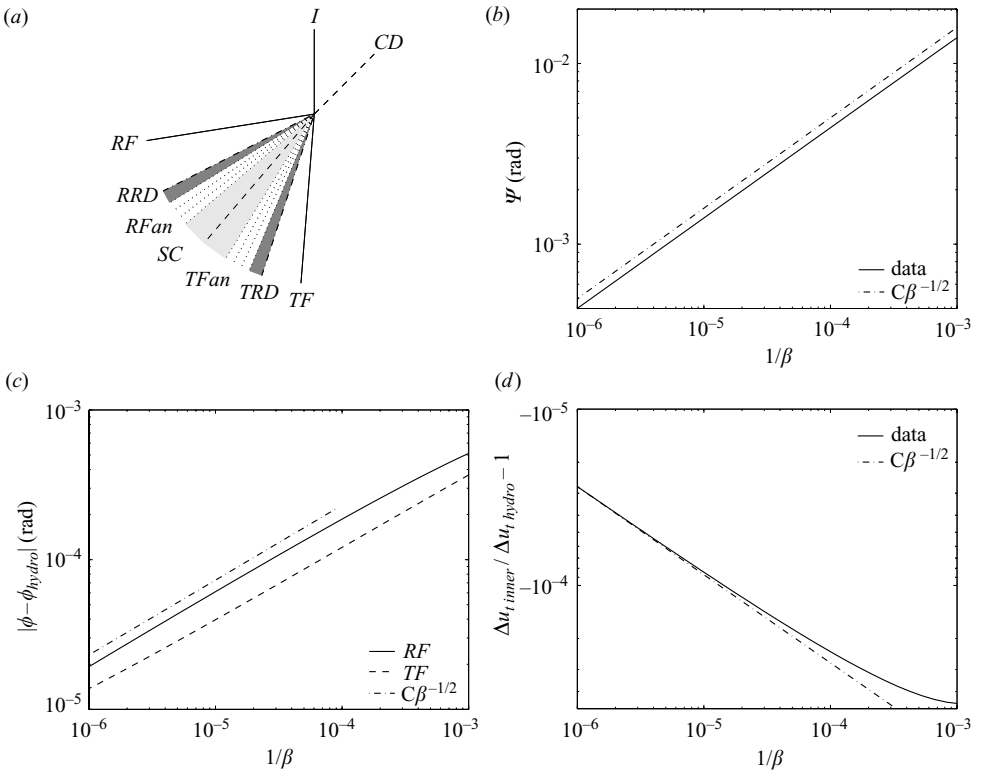


FIGURE 13. (*a*) Illustration of the septuple-point flow structure. The angular separations of the RDs and fans along with the angular extent of the fans have been exaggerated for clarity. (*b*) Variation of the angular width of the inner layer Ψ with β^{-1}. (*c*) Deviation of the angles of shocks *RF* and *TF* from their hydrodynamic triple-point values, ϕ_{hydro}, versus β^{-1}. (*d*) β^{-1} dependence of the tangential velocity jump across the inner layer, $\Delta u_{t\,inner}$, normalized by the tangential velocity jump across the *SC* in the corresponding hydrodynamic triple-point solution, $\Delta u_{t\,hydro}$. Logarithmic axes are used for (*b*)–(*d*) to illustrate the power-law dependence of the plotted quantities on β^{-1}. Sample power-law curves are included for comparison.

solution, $\Delta u_{t\,hydro}$. This reveals that as β becomes large, $\Delta u_{t\,inner}$ converges to $\Delta u_{t\,hydro}$. These observations suggest that, in the limit as $\beta \to \infty$, the septuple-point solution is identical to the hydrodynamic triple-point solution, with the exception that the hydrodynamic CD is replaced by the inner layer. The density and tangential velocity jumps across the inner layer, which are equal to those across the hydrodynamic CD in the limit, are supported by different elements within the layer. The density jump is principally supported by the MHD CD, but as this cannot support a shear, the tangential velocity jump must be supported by the RDs and expansion fans. Profiles of the tangential velocity within the inner layer for $\beta \approx 10.56$ and $\beta \approx 255\,306$ are shown in figure 14. These demonstrate that for moderate β, the tangential velocity jump is principally supported by the RDs, while for large β, it is almost entirely supported by the expansion fans. This is because the tangential velocity jump across an RD scales as $(\sqrt{\gamma\,\rho/p}\,\beta\,M_{Sn})^{-1}$, which can be derived from (A 12). From our results, we also observe that for large β, each expansion fan supports finite jumps in ρ, p and B_t to balance the tangential velocity jump. This implies that while B_t tends to zero outside of the inner layer, it remains finite downstream of the expansion fans. Further, figure 14 shows that for large β, the angular extents of fans *RFan* and *TFan*

https://doi.org/10.1017/S0022112004001880 Published online by Cambridge University Press

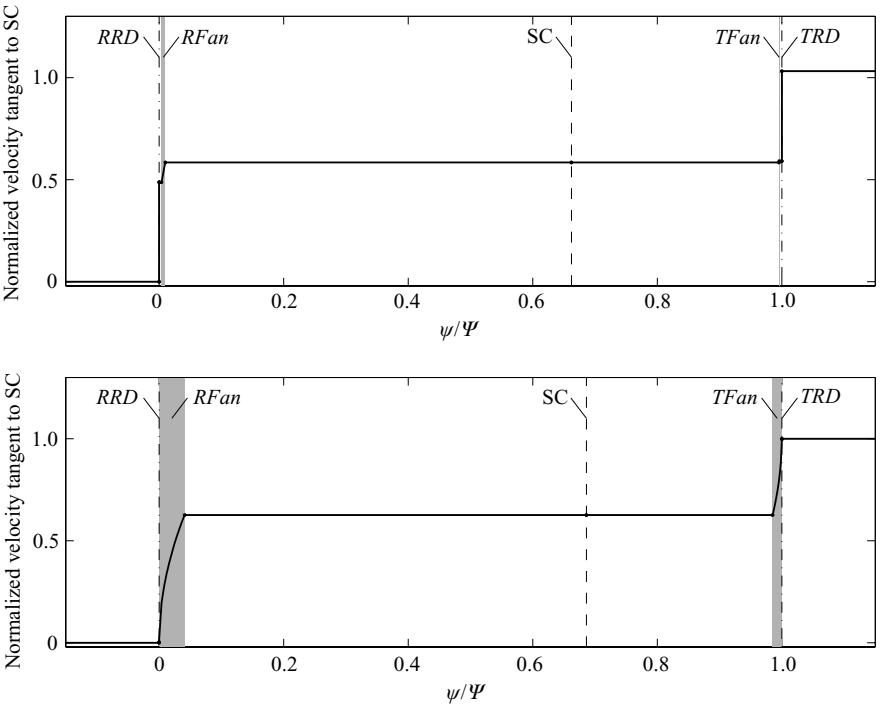


FIGURE 14. Velocity profiles within the inner layer of the septuple-point solution for two values of β along Branch Ir. The plotted velocity component is tangential to the SC and has been normalized such that it is zero at $\psi = 0$ and unity at $\psi = \Psi$. The top profile is for $\beta \approx 10.56$ and the bottom profile is for $\beta \approx 255\,606$. The angle ψ is defined counterclockwise from RRD.

still consume a finite fraction of the width of the inner layer. These findings indicate that in the limit of β tending to infinity, the inner layer is a singular structure.

6.2. *Behaviour of quintuple-point solutions at large* β

The structure of the quintuple-point c-solution is illustrated in figure 15(a). In the quintuple-point solution, RF and TF are fast shocks while RS and TS are C_1 compound waves labelled RC_1 and TC_1, respectively. We will refer to the expansion fan portions of RC_1 and TC_1 as *RFan* and *TFan*, respectively. Following Branch Ic revealed that the quintuple-point flow structure is maintained up to the highest β values for which solutions were computed. We discontinued following Branch Ic after establishing that its behaviour is practically identical to that of Branch Ir. The reason that Branch Ic was not followed to the same β_{max} as Branch Ir is that solutions along this sub-branch are much more computationally expensive to calculate for large β. The additional expense arises from computing the angles of the $2 \rightarrow 3 = 4$ intermediate shocks. Computing these angles requires (C 1) to be solved iteratively. For large β, we observe that the coefficients $\mathscr{B}$, $\mathscr{C}$ and $\mathscr{D}$ in this equation approximately scale as β. Thus, the terms in (C 1) approximately scale as β^3 as they involve triple products of these coefficients. Satisfying (C 1) to the same absolute tolerance for all β therefore requires the working precision of the iterative scheme to be increased like β^3, as the terms become large, greatly increasing the computational expense.

Figures 15(b) and 15(c) show comparisons of Ψ and the fast shock angles from Branches Ic and Ir. These demonstrate that the behaviour of the quintuple-point and septuple-point solutions is practically identical, despite the structural differences

https://doi.org/10.1017/S0022112004001880 Published online by Cambridge University Press

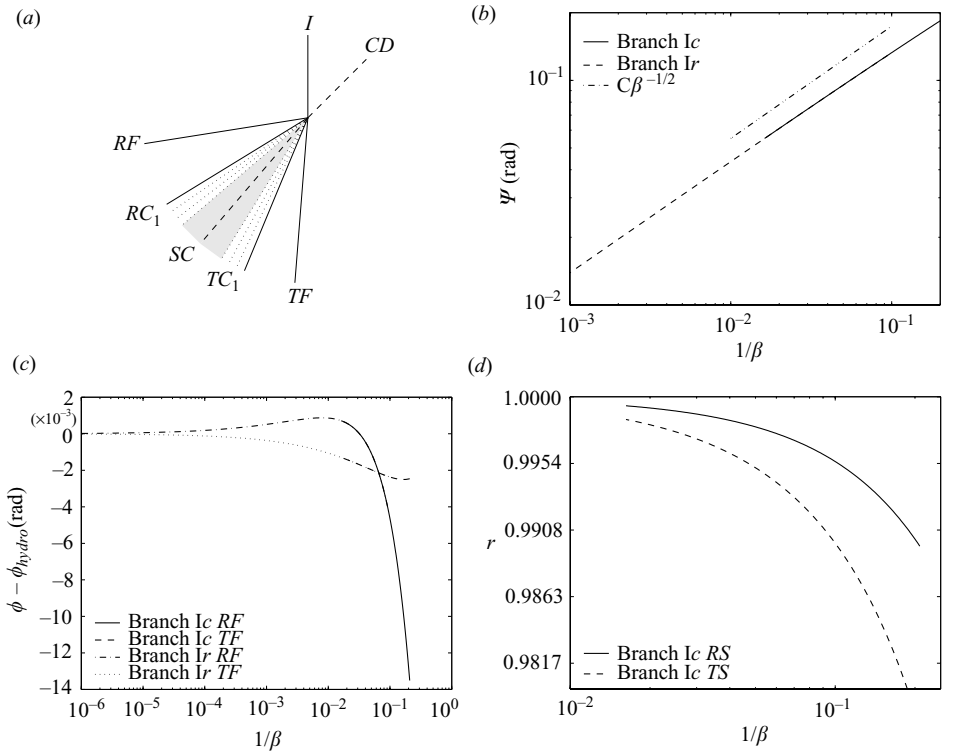


FIGURE 15. (*a*) Illustration of the quintuple-point flow structure. (*b*) Variation of the angular width of the inner layer Ψ with β^{-1} for Branches I*c* and I*r*. (*c*) Deviation of the angles of shocks *RF* and *TF* from their hydrodynamic triple-point values, ϕ_{hydro}, versus β^{-1} for Branches I*c* and I*r*. (*d*) β^{-1} dependence r for the transmitted and reflected $2 \rightarrow 3 = 4$ intermediate shocks, denoted *RI* and *TI*, respectively, along Branch I*c*.

between the two solutions. Figure 15(*d*) shows how the values of r for the reflected and transmitted $2 \rightarrow 3 = 4$ intermediate shocks vary with increasing β. It suggests that for large β, r tends toward unity for both shocks while they continue to reverse the sign of B_t as they are of an intermediate shock-type. This indicates that the $2 \rightarrow 3 = 4$ intermediate shocks reproduce the behaviour of the RDs in the septuple-point for large β, implying that in the limit of β tending to infinity, the tangential velocity jump across the inner layer is supported by *RFan* and *TFan*. Additionally, figure 15(*b*) shows that the angular width of the inner layer scales as $\beta^{-1/2}$; hence, the angular extents of *RFan* and *TFan* tend to zero for large β, as in the septuple-point solution. These results show that in the limit of β tending to infinity, the inner layer of the quintuple-point solution is also a singular structure as the expansion fans support finite jumps in u_t, B_t, ρ and p while their angular extents tend to zero. We will now investigate this singular structure in more detail.

7. Structure of the singular wedge

7.1. *Rescaling within the singular wedge*

In the septuple-point solution, we denote the angle between *RRD* and the leading wavelet of *RFan* as $\Delta\psi_1$, the angular extent of *RFan* as $\Delta\psi_2$, the angle between the

https://doi.org/10.1017/S0022112004001880 Published online by Cambridge University Press

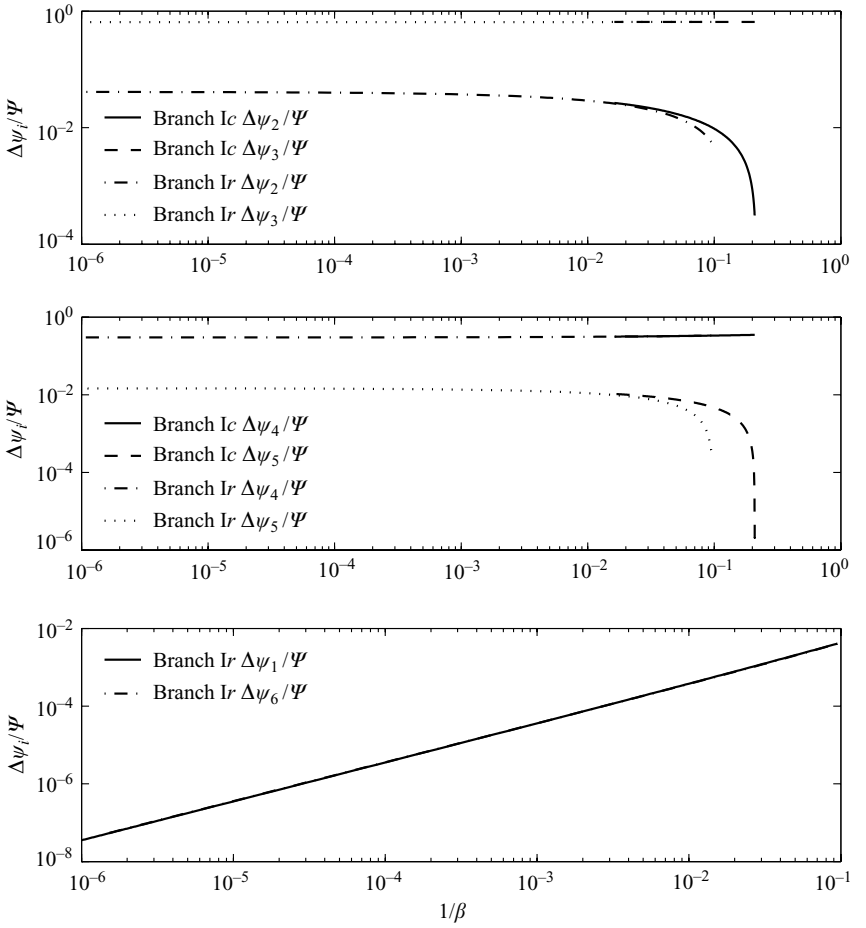


FIGURE 16. Variation of the sector widths within the inner layer along Branches I*c* and I*r*.

last wavelet of *RFan* and the SC as $\Delta\psi_3$, the angle between the SC and the last wavelet of *TFan* as $\Delta\psi_4$, the angular extent of *TFan* as $\Delta\psi_5$, and the angle between the leading wavelet of *TFan* and *TRD* as $\Delta\psi_6$. In the quintuple-point solution, $\Delta\psi_2$-$\Delta\psi_5$ are defined in the same way while $\Delta\psi_1$ and $\Delta\psi_6$ are both zero. Figure 16 shows how these sector widths vary with β^{-1} along Branches I*c* and I*r*. For both branches, each of $\Delta\psi_2/\Psi$, $\Delta\psi_3/\Psi$, $\Delta\psi_4/\Psi$ and $\Delta\psi_5/\Psi$ asymptote to constant values for large β, indicating that these sector widths have the same $\beta^{-1/2}$ scaling as Ψ. Note that each of these scaled sector widths appear to asymptote to the same value for both branches. For the septuple-point solution, both $\Delta\psi_1$ and $\Delta\psi_6$ scale as β^{-1}; hence, they are small when compared to the other sector widths in the limit of large β. Further interrogation of the solutions along Line I revealed that within the inner layer (i.e. downstream of *RFan* and *TFan*), M_{Sn} and K_n scale as $\beta^{-1/2}$ for large β. Conversely, ρ, p, M_{St} and K_t remain finite. This implies that even as $\beta \to \infty$, the magnetic field within the inner layer is finite and scales like $\sqrt{\mu_0 p_3}$. In addition, the SC cannot support a tangential velocity jump as the magnetic field is not parallel to it.

https://doi.org/10.1017/S0022112004001880 Published online by Cambridge University Press

The observed dependence of the inner-layer flow states on β suggests the following expansions in terms of the small parameter $\varepsilon \equiv \beta^{-1/2}$:

$$M_{Sn}(\zeta;\varepsilon) = \varepsilon M_{Sn}^{(1)}(\zeta) + \varepsilon^2 M_{Sn}^{(2)}(\zeta) + O(\varepsilon^3), \tag{7.1}$$

$$M_{St}(\zeta;\varepsilon) = M_{St}^{(0)}(\zeta) + \varepsilon M_{St}^{(1)}(\zeta) + O(\varepsilon^2), \tag{7.2}$$

$$K_n(\zeta;\varepsilon) = \varepsilon K_n^{(1)}(\zeta) + \varepsilon^2 K_n^{(2)}(\zeta) + O(\varepsilon^3), \tag{7.3}$$

$$K_t(\zeta;\varepsilon) = K_t^{(0)}(\zeta) + \varepsilon K_t^{(1)}(\zeta) + O(\varepsilon^2), \tag{7.4}$$

$$\rho(\zeta;\varepsilon) = \rho^{(0)}(\zeta) + \varepsilon \rho^{(1)}(\zeta) + O(\varepsilon^2), \tag{7.5}$$

where $\zeta \equiv \psi/\varepsilon$. For each expansion fan, ζ originates from the leading wavelet and increases in the downstream direction. Substituting these expansions into (B 9)–(B 13), we obtain the following set of coupled differential equations in ζ for the leading-order terms within *RFan* and *TFan*:

$$\frac{\mathrm{d}\rho^{(0)}}{\mathrm{d}\zeta} = \rho^{(0)} f_\rho, \tag{7.6}$$

$$\frac{\mathrm{d}M_{Sn}^{(1)}}{\mathrm{d}\zeta} = -\left(\frac{\gamma+1}{2} M_{Sn}^{(1)} f_\rho + M_{St}^{(0)}\right), \tag{7.7}$$

$$\frac{\mathrm{d}M_{St}^{(0)}}{\mathrm{d}\zeta} = -\left(\frac{\gamma}{2}\frac{M_{Sn}^{(1)}}{K_n^{(1)}K_t^{(0)}} + \frac{K_t^{(0)}}{K_n^{(1)}} M_{Sn}^{(1)} + \frac{\gamma-1}{2} M_{St}^{(0)}\right) f_\rho, \tag{7.8}$$

$$\frac{\mathrm{d}K_n^{(1)}}{\mathrm{d}\zeta} = -\left(\frac{\gamma}{2} K_n^{(1)} f_\rho + K_t^{(0)}\right), \tag{7.9}$$

$$\frac{\mathrm{d}K_t^{(0)}}{\mathrm{d}\zeta} = -\frac{\gamma}{2}\left(\frac{1}{K_t^{(0)}} + K_t^{(0)}\right) f_\rho, \tag{7.10}$$

where,

$$f_\rho = \frac{-2M_{Sn}^{(1)} M_{St}^{(0)}\left(1 + (2/\gamma)K_t^{(0)2}\right) + (4/\gamma)K_n^{(1)}K_t^{(0)}}{\left[\gamma + 3 + (4 + 2/\gamma)K_t^{(0)2}\right] M_{Sn}^{(1)2} - 2K_n^{(1)2}}.$$

The source of the observed singular change in the tangential magnetic field across each expansion fan is the term involving $1/K_t^{(0)}$ in (7.10). At the leading wavelet of an expansion fan, where $K_t^{(0)} = 0$, this causes the ζ-derivative of $K_t^{(0)}$ to be infinite. Within the expansion fans, we find that to leading order in ζ, $K_t^{(0)}$ behaves like $\sqrt{\zeta}$ near $\zeta = 0$.

Computing the leading-order asymptotic approximation to the inner-layer structure in the limit of large β requires (7.6)–(7.10) to be solved. To achieve this, boundary conditions for each of these equations are necessary. The boundary conditions for the $O(1)$ quantities $\rho^{(0)}$, $M_{St}^{(0)}$ and $K_t^{(0)}$ are the values on either side of the SC in the corresponding hydrodynamic triple-point solution (zero in the case of $K_t^{(0)}$). Obtaining boundary conditions for $M_{Sn}^{(1)}$ and $K_n^{(1)}$ requires the $O(\varepsilon)$ quantities outside of the inner layer to be computed. In Appendix E, we show that the $2 \to 3 = 4$ intermediate shocks in the quintuple-point solution and the RDs in the septuple-point solution do not affect the boundary conditions for (7.6)–(7.10) and hence are omitted from the leading-order solution. Combined with other arguments, this implies that the leading-order asymptotic solution is the large β limit of both the quintuple-point and septuple-point solutions.

https://doi.org/10.1017/S0022112004001880 Published online by Cambridge University Press

7.2. *Equations for $O(\varepsilon)$ quantities outside the singular wedge*

In each region outside of the inner layer, ρ, p and $\boldsymbol{u}$ can be expanded about their values in the triple-point solution, which are denoted with the superscript (0). For example,

$$\rho(\phi;\,\varepsilon) = \rho^{(0)}(\phi) + \varepsilon\rho^{(1)}(\phi) + O(\varepsilon^2).$$

From the definition of ε, the appropriate expansion for the magnetic field is

$$\boldsymbol{B}(\phi;\,\varepsilon) = \varepsilon\boldsymbol{B}^{(1)}(\phi) + O(\varepsilon^2).$$

As I is a hydrodynamic shock, the presence of $\boldsymbol{B}$ does not perturb the hydrodynamic variables in region 1. Thus, $\rho_1 = \rho_1^{(0)}$, $p_1 = p_1^{(0)}$ and $\boldsymbol{B}_1 = \varepsilon\boldsymbol{B}_{1nu}^{(1)}\hat{\boldsymbol{e}}_x = -\varepsilon(2\,\mu_0 p_0)^{1/2}\,\hat{\boldsymbol{e}}_x$. Here, $\hat{\boldsymbol{e}}_x$ is a unit vector oriented in the x-direction. From our examination of Branch Ir, we observe that the fast shock angles are perturbed about their triple-point values as follows:

$$\phi = \phi^{(0)} + \varepsilon\phi^{(1)} + O(\varepsilon^2).$$

This perturbs the velocity components upstream of RF and TF about their triple-point values. We will denote vector components defined relative to plane waves forming the upstream and downstream boundaries of a region with the subscripts u and d, respectively. The perturbed velocity components immediately upstream of RF are given by

$$\begin{aligned}
u_{1nd} &= u_{1nd}^{(0)} + \varepsilon u_{1nd}^{(1)} + O(\varepsilon^2)\\
&= -u_{1tu}^{(0)}\cos\phi_1^{(0)} - u_{1nu}^{(0)}\sin\phi_1^{(0)} + \varepsilon\phi_1^{(1)}\left(u_{1tu}^{(0)}\sin\phi_1^{(0)} - u_{1nu}^{(0)}\cos\phi_1^{(0)}\right) + O(\varepsilon^2),\\
u_{1td} &= u_{1td}^{(0)} + \varepsilon u_{1td}^{(1)} + O(\varepsilon^2)\\
&= -u_{1tu}^{(0)}\sin\phi_1^{(0)} + u_{1nu}^{(0)}\cos\phi_1^{(0)} - \varepsilon\phi_1^{(1)}\left(u_{1tu}^{(0)}\cos\phi_1^{(0)} + u_{1nu}^{(0)}\sin\phi_1^{(0)}\right) + O(\varepsilon^2),
\end{aligned}$$

while the $O(\varepsilon)$ magnetic field components are given by

$$\begin{aligned}
B_{1nd} &= \varepsilon B_{1nd}^{(1)} = -\varepsilon B_{1nu}^{(1)}\sin\phi_1^{(0)},\\
B_{1td} &= \varepsilon B_{1td}^{(1)} = \varepsilon B_{1nu}^{(1)}\cos\phi_1^{(0)}.
\end{aligned}$$

The $O(\varepsilon)$ vector components upstream of TF are calculated in a similar manner.

The magnetic field just downstream of the fast shocks will also be $O(\varepsilon)$ because the shocks are not close to the switch-on limit. To compute the perturbed flow-states downstream of RF and TF ($2u$ and $4u$, respectively), shock jump conditions for the $O(\varepsilon)$ quantities are required. These are obtained by substituting our expansions for ρ, p, $\boldsymbol{u}$ and $\boldsymbol{B}$ into (2.6)–(2.10) in the reference frame where $u_t^{(0)} = 0$. By setting the $O(1)$ terms of the resulting expressions equal to zero, we obtain the usual hydrodynamic shock jump conditions. Setting the $O(\varepsilon)$ terms equal to zero yields

$$\left[\rho^{(0)}u_n^{(1)} + \rho^{(1)}u_n^{(0)}\right] = 0, \tag{7.11}$$

$$\left[2\rho^{(0)}u_n^{(0)}u_n^{(1)} + \rho^{(1)}u_n^{(0)2} + p^{(1)}\right] = 0, \tag{7.12}$$

$$\left[u_t^{(1)}\right] = 0, \tag{7.13}$$

$$\left[\frac{\left(\rho^{(1)}u_n^{(0)} + 3\rho^{(0)}u_n^{(1)}\right)u_n^{(0)2}}{2} + \frac{\gamma\left(u_n^{(1)}p^{(0)} + u_n^{(0)}p^{(1)}\right)}{\gamma - 1}\right] = 0, \tag{7.14}$$

$$\left[u_n^{(0)}B_t^{(1)}\right] = 0. \tag{7.15}$$

https://doi.org/10.1017/S0022112004001880 Published online by Cambridge University Press

These equations are not valid for shocks that are almost switch-on shocks. The values of $\rho^{(1)}$, $p^{(1)}$ and $u_n^{(1)}$ downstream of each fast shock are obtained by the simultaneous solution of (7.11), (7.12) and (7.14). Once $u_n^{(1)}$ is known on both sides of each shock, the downstream values of $B_t^{(1)}$ can be computed from (7.15). Equation (7.13) shows that $u_t^{(1)}$ is continuous across each shock, as is $B_n^{(1)}$.

To compute the $O(\varepsilon)$ components of flow-states $2d$ and $4d$, which are defined relative to the leading wavelets of *RFan* and *TFan*, respectively, we must first compute the $O(1)$ and $O(\varepsilon)$ terms in the expansions for $\Delta\phi_d$ (the angle between *RF* and *RFan*) and $\Delta\phi_a$ (the angle between *TF* and *TFan*). This can be accomplished by substituting our expansions for the primitive variables into (D 2) because we determined that the location of each leading wavelet is the same as that of an RD up to $O(\varepsilon)$. For $\Delta\phi_d$, this gives

$$\begin{aligned}\Delta\phi_d &= \Delta\phi_d^{(0)} + \varepsilon\Delta\phi_d^{(1)} + O(\varepsilon^2)\\ &= \arctan\frac{M_{Sn}^{(0)}}{M_{St}^{(0)}} + \frac{\varepsilon M_{Sn}^{(0)} M_{St}^{(0)}}{M_{Sn}^{(0)^2} + M_{St}^{(0)^2}}\left[\frac{M_{Sn}^{(1)}}{M_{Sn}^{(0)}} - \frac{M_{St}^{(1)}}{M_{St}^{(0)}} - \sqrt{\frac{2}{\gamma}}\left(\frac{K_n^{(1)}}{M_{Sn}^{(0)}} - \frac{K_t^{(1)}}{M_{St}^{(0)}}\right)\right] + O(\varepsilon^2),\end{aligned}$$

where the subscript $2u$ has been dropped from all quantities for clarity and

$$K_{n/t}^{(1)} = \frac{B_{n/t}^{(1)}}{\sqrt{2\mu_0 p^{(0)}}}, \tag{7.16}$$

$$M_{Sn/t}^{(1)} = M_{Sn/t}^{(0)}\left(\frac{u_{n/t}^{(1)}}{u_{n/t}^{(0)}} + \frac{\rho^{(1)}}{2\rho^{(0)}} - \frac{p^{(1)}}{2p^{(0)}}\right). \tag{7.17}$$

Note that $\Delta\phi_d^{(0)}$ is equal to the angle between the reflected shock and the SC in the corresponding triple-point solution, a prerequisite for the $O(1)$ terms in our expansions corresponding to a triple-point solution. $\Delta\phi_a^{(1)}$ is computed by inserting flow-state $4u$ into the above relation for $\Delta\phi_d^{(1)}$ and inverting the direction of $\boldsymbol{K}_{4u}^{(1)}$. We can now compute $u_{2nd}^{(1)}$ using

$$u_{2nd}^{(1)} = -\Delta\phi_d^{(1)} u_{2td}^{(0)} + u_{2nu}^{(1)}\cos\Delta\phi_d^{(0)} - u_{2tu}^{(1)}\sin\Delta\phi_d^{(0)}.$$

A similar relation is used to compute $u_{4nd}^{(1)}$. From the hydrodynamic triple-point solution, both $u_{2nd}^{(0)}$ and $u_{4nd}^{(0)}$ are zero. This results in the inner-layer boundary conditions for M_{Sn} being $O(\varepsilon)$, as required by (7.7). The leading-order magnetic field components upstream of *RFan* are given by

$$\begin{aligned}B_{2nd}^{(1)} &= B_{2nu}^{(1)}\cos\Delta\phi_d^{(0)} - B_{2tu}^{(1)}\sin\Delta\phi_d^{(0)},\\ B_{2td}^{(1)} &= B_{2nu}^{(1)}\sin\Delta\phi_d^{(0)} + B_{2tu}^{(1)}\cos\Delta\phi_d^{(0)}.\end{aligned}$$

The components upstream of *TFan* are computed in the same manner.

The boundary conditions for (7.6)–(7.10) can now be computed from states $2d$ and $4d$ upstream of the fans; the boundary conditions for $\rho^{(0)}$, $p^{(0)}$ and $M_{St}^{(0)}$ are taken directly from the triple-point solution on either side of the shocked interface. Equation (7.16) is used to calculate the boundary conditions for $K_n^{(1)}$ from states $2d$ and $4d$ while the boundary conditions for $M_{Sn}^{(1)}$ are computed using

$$M_{S2nd}^{(1)} = \frac{u_{2nd}^{(1)}}{\sqrt{\gamma p_2^{(0)}/\rho_2^{(0)}}}, \quad M_{S4nd}^{(1)} = \frac{u_{4nd}^{(1)}}{\sqrt{\gamma p_4^{(0)}/\rho_4^{(0)}}}.$$

Finally, the appropriate boundary conditions for $K_t^{(0)}$ are zero.

https://doi.org/10.1017/S0022112004001880 Published online by Cambridge University Press

7.3. *Leading-order matching conditions at the interface*

The leading-order terms of flow-state $3u$ immediately downstream of the trailing wavelet of *RFan* are computed by numerically integrating (7.6)–(7.10) from $\zeta = 0$ to $\zeta = \Delta\zeta_2 \equiv \Delta\psi_2/\varepsilon$ using the boundary conditions derived in § 7.2. Similarly, flow-state $5u$ is computed by numerically integrating (7.6)–(7.10) from $\zeta = 0$ to $\zeta = \Delta\zeta_5 \equiv \Delta\psi_5/\varepsilon$. To leading order, the angular separations between the trailing wavelets of the expansion fans and the SC, $\varepsilon\Delta\zeta_3$ and $\varepsilon\Delta\zeta_4$, are given by

$$\Delta\zeta_3 = \frac{u^{(1)}_{3nu}}{u^{(0)}_{3tu}}, \quad \Delta\zeta_4 = \frac{u^{(1)}_{5nu}}{u^{(0)}_{5tu}}.$$

Using this, it can be shown that the leading-order matching conditions for pressure, velocity magnitude, velocity direction, tangential magnetic field and normal magnetic field can be expressed as

$$p^{(0)}_3 = p^{(0)}_5, \tag{7.18}$$

$$u^{(0)}_{3tu} = u^{(0)}_{5tu}, \tag{7.19}$$

$$\phi^{(1)}_1 + \Delta\phi^{(1)}_d + \Delta\zeta_2 + \Delta\zeta_3 + \Delta\zeta_4 + \Delta\zeta_5 - \phi^{(1)}_3 + \Delta\phi^{(1)}_a = 0, \tag{7.20}$$

$$K^{(0)}_{3tu} = K^{(0)}_{5tu}, \tag{7.21}$$

$$K^{(1)}_{3nu} - \Delta\zeta_3 K^{(0)}_{3tu} + K^{(1)}_{5nu} - \Delta\zeta_4 K^{(0)}_{5tu} = 0. \tag{7.22}$$

7.4. *Leading-order asymptotic solution technique*

The leading-order asymptotic solution is computed in the same manner as the solution to the full problem. The solution can be completely specified by four scaled angles, $\phi^{(1)}_1$, $\phi^{(1)}_3$, $\Delta\zeta_2$ and $\Delta\zeta_5$. An approximate solution is found by iterating on these four angles using a secant method until (7.18)–(7.21) are satisfied to eight significant figures. To check the consistency of this procedure, the final angles are substituted into (7.22) to ensure that it is satisfied to the same precision. It was found that the radius of convergence for this set of equations is very small, necessitating extremely accurate initial guesses for the four angles to achieve a converged solution. One difficulty that arises in this problem is that the derivatives in (7.8) and (7.10) are infinite at the leading wavelet of each expansion fan ($\zeta = 0$) as they contain terms involving $1/K^{(0)}_t$. Thus, they cannot be integrated numerically if the physical boundary condition $K^{(0)}_t = 0$ is used. This is handled by setting the boundary conditions on $K^{(0)}_t$ to be the small values $-\epsilon K^{(1)}_{2td}$ and $-\epsilon K^{(1)}_{4td}$ at the leading wavelets of *RFan* and *TFan*, respectively. The value of ϵ used was 10^{-10}. This procedure is acceptable because in the immediate vicinity of the leading wavelet ($\zeta \ll 1$), the growth of $K^{(0)}_t$ is decoupled to leading order (in ζ) from changes in the other variables. For $\zeta \ll 1$, $K^{(0)}_t$ behaves like $\sqrt{\zeta}$ to leading order while the other variables are constant to leading order.

7.5. *Comparing the full and asymptotic solutions*

We have computed the leading-order asymptotic solution to the shock refraction problem specified by the parameters defining Line I, which are given in table 1. For this set of parameters, we found that $\phi^{(1)}_1 = 0.01981083$, $\phi^{(1)}_3 = -0.01205304$, $\Delta\zeta_2 = 0.01814016$, and $\Delta\zeta_5 = 0.00646063$. The residual of (7.22) is less than 10^{-9} for the set of angles computed.

Approximate values for $O(\varepsilon)$ terms can be recovered from the full solutions along Branches I*c* and I*r*. For example, an approximate value for $\phi^{(1)}_1$ can be computed

https://doi.org/10.1017/S0022112004001880 Published online by Cambridge University Press

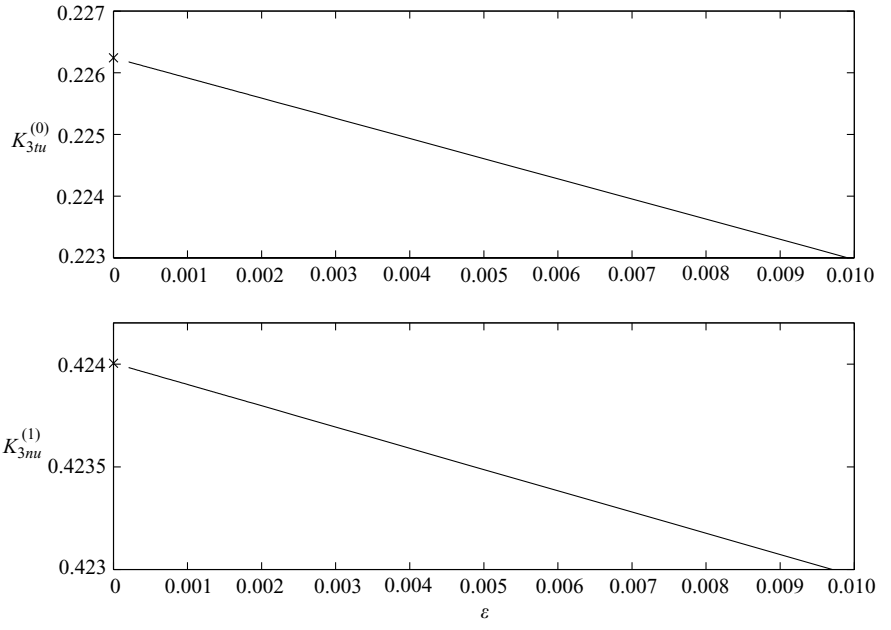


FIGURE 17. $K_{3t}^{(0)}$ and $K_{3n}^{(1)}$ values from the leading-order asymptotic solution ($\times$) and approximated from Branch Ir ($-$) versus ε.

using

$$\phi_{1\,approx}^{(1)} = \frac{\phi_1 - \phi_1^{(0)}}{\varepsilon},$$

where ϕ_1 and ε are taken from a full solution along either Branch Ic or Branch Ir. Note that these approximations have an error proportional to the value of ε for the full solution used. The approximate values of $\phi_1^{(1)}$, $\phi_3^{(1)}$, $\Delta\zeta_2$ and $\Delta\zeta_5$ from Branch Ir were extrapolated to $\varepsilon = 0$ and compared to the values from the leading-order asymptotic solution. The relative errors were found to be at most 7.7×10^{-6}, which is an order of magnitude less than the smallest value of ε from Branch Ir. Figure 17 shows a comparison between the values of representative $O(1)$ and $O(\varepsilon)$ inner-layer quantities from the asymptotic solution and approximated from Branch Ir. In general, there was found to be excellent agreement between the leading-order asymptotic solution and the full solutions at the end of Branch Ir in the limit of small ε.

8. Conclusions

We have developed an iterative procedure for determining the ideal magnetohydrodynamic flow structure produced by the regular refraction of a shock at an oblique planar density interface with a density ratio larger than unity. This procedure was used to reproduce the quintuple-point structure observed in the numerical simulations of Samtaney (2003). The quintuple-point structure is similar to the hydrodynamic triple-point, but with the SC replaced with two sub-fast shocks bracketing an MHD CD. The features of this structure were described in detail and excellent agreement was found between our results and those of Samtaney (2003). For Samtaney's conditions, one of the sub-fast shocks is a $2 \rightarrow 4$ intermediate shock. A second solution was computed

https://doi.org/10.1017/S0022112004001880 Published online by Cambridge University Press

in which the intermediate shock was replaced by a 180° rotational discontinuity followed downstream by a slow shock. This is referred to as a regular solution while the quintuple-point structure involving the intermediate shock is referred to as being irregular. For the three-dimensional ideal MHD equations, all waves that appear in regular solutions are admissible under the evolutionary condition according to Falle & Komissarov (2001). While for the strongly planar ideal MHD equations, in which gradients and vectors are restricted to a plane (in some reference frame), all waves that appear in irregular solutions are admissible under the evolutionary condition.

For four sets of parameters, regular and irregular solution branches corresponding to increasing β were traced. It was found that as β is increased, the two shocks bracketing the SC undergo a number of transitions. Along each regular branch, the initial transitions are from slow shocks to 180° rotational discontinuities followed downstream by slow shocks. As β is increased further, these transition to 180° rotational discontinuities followed downstream by slow-mode expansion fans. Along each irregular solution branch, the transitions are from slow shocks to $2 \rightarrow 4$ intermediate shocks and finally to C_1 compound waves with increasing β.

Once all transitions are complete, we identified two possible flow structures that may arise from the shock refraction process: an irregular quintuple-point solution consisting of a hydrodynamic shock, two fast shocks, and two C_1 compound waves, and a seven wave regular solution consisting of a hydrodynamic shock, two fast shocks, two 180° rotational discontinuities, and two slow-mode expansion fans, along with the contact discontinuity. The seven wave structure is denoted the septuple-point solution. The quintuple-point and septuple-point solutions remain valid up to the largest β values investigated using the iterative procedure. Our results suggest that in the limit of infinite β, both solutions become identical to the hydrodynamic triple-point solution, with the exception that the shocked hydrodynamic contact is replaced by a singular structure we call the inner layer. The inner layer is a wedge bounded by either the two compound waves or the two rotational discontinuities followed by the two slow-mode expansion fans. These bracket MHD contact. In both cases, the angle of this wedge scales as $\beta^{-1/2}$, which is proportional to the applied magnetic field magnitude. A scaling for each of the variables within the inner layer is suggested from the results of our computations. Significantly, this scaling implies that the magnetic field within the inner layer is finite in the limit of β tending to infinity. In addition, the magnetic field is not parallel to the MHD contact, hence it cannot support a jump in tangential velocity. This necessitates the presence of the expansion fans (which are part of the compound waves in the quintuple-point solution), which support the tangential velocity discrepancy across the inner layer even though their angular extents tend to zero. To verify these findings, the equations governing the leading-order asymptotic solution of the shock refraction problem in the limit of large β were derived. These equations were then solved iteratively. We argue that the leading-order asymptotic solution is the large β limit of both the quintuple-point and septuple-point solutions, in part because neither the shock portions of the compound waves nor the rotational discontinuities participate in it. The asymptotic and full solutions were compared quantitatively and there was found to be excellent agreement between the two.

The authors wish to thank Professor S. A. E. G. Falle of the University of Leeds for his useful comments and suggestions. V. W. and D. I. P. are supported by the Academic Strategic Alliances Program of the Accelerated Strategic Computing Initiative (ASCI/ASAP) under subcontract no. B341492 of DOE contract W-7405-ENG-48. R. S. is supported under the DOE SciDAC program (USDOE contract

https://doi.org/10.1017/S0022112004001880 Published online by Cambridge University Press

no. DE-AC020-76-CH03073). This research used resources of the National Energy Research Scientific Computing Center, which is supported by the Office of Science of the US Department of Energy under contract no. DE-AC03-76SF00098.

Appendix A. The MHD Rankine–Hugoniot relations

Solutions to the MHD RH relations can be found as follows. It can then be shown that equations (2.6)–(2.9) reduce to the following algebraic equation in r and b obtained by Liberman & Velikhovich (1986):

$$F(r,b) = Ar^2 + Br + C = 0, \tag{A 1}$$

where

$$A = -\frac{1}{2}\frac{\gamma+1}{\gamma-1}, \qquad B = \frac{1}{(\gamma-1)M_{S1}^2} + \frac{\gamma}{(\gamma-1)}\left(1 - \frac{b^2-\sin^2\theta_1}{2M_{A1}^2}\right), \tag{A 2}$$

$$C = -\frac{1}{2} - \frac{1}{(\gamma-1)M_{S1}^2} + \frac{b^2-\sin^2\theta_1 - Y\,(b-\sin\theta_1)^2}{2M_{A1}^2}, \qquad Y = 1 - \frac{1}{M_{I1}^2}. \tag{A 3}$$

The relation $F(r,b)=0$ defines a curve in (r,b) space on which the fluxes of mass, momentum and energy are equal to those upstream of the shock. The final jump condition can be expressed as

$$Z(r,b) = bX - Y\sin\theta_1 = 0, \tag{A 4}$$

where

$$X = r - \frac{1}{M_{I1}^2}. \tag{A 5}$$

The intersections of the curves defined by $F=0$ and $Z=0$ are the locations in (r,b) space where all jump conditions are satisfied. The two equations $F=0$ and $Z=0$ are combined into a quartic equation in r, which is then divided by the known factor $(r-1)$ to yield the cubic

$$\mathscr{R}(r) = \mathscr{A}r^3 + \mathscr{B}r^2 + \mathscr{C}r + \mathscr{D} = 0, \tag{A 6}$$

where

$$\mathscr{A} = \frac{\gamma+1}{\gamma-1},$$

$$\mathscr{B} = -1 - \frac{2}{(\gamma-1)\,M_{S1}^2} - \frac{2\,(\gamma+1)\cos^2(\theta_1) + \gamma\sin^2(\theta_1)}{(\gamma-1)\,M_{A1}^2},$$

$$\mathscr{C} = \frac{(\gamma+1)\,M_{S1}^2 + \left[4 + M_{S1}^2\,(3\gamma-4)\right]M_{A1}^2 + \left[(\gamma+1)\,M_{S1}^2 + \left(4+M_{S1}^2\gamma\right)M_{A1}^2\right]\cos(2\theta_1)}{2\,(\gamma-1)\,M_{A1}^4 M_{S1}^2},$$

$$\mathscr{D} = -\frac{\left[1 + (\gamma-1)\,M_{S1}^2 + \cos(2\theta_1)\right]\cos^2(\theta_1)}{(\gamma-1)\,M_{A1}^4 M_{S1}^2}.$$

In terms of these coefficients, the roots of the cubic, referred to hereinafter as roots

https://doi.org/10.1017/S0022112004001880 Published online by Cambridge University Press

A, B and C, can be expressed as

$$r_A = \frac{1}{6\mathscr{A}}[-2\mathscr{B} + J + H], \tag{A 7}$$

$$r_B = \frac{1}{12\mathscr{A}}[-4\mathscr{B} - (H + J) + \sqrt{3}\,\mathrm{i}\,(H - J)], \tag{A 8}$$

$$r_C = \frac{1}{12\mathscr{A}}[-4\mathscr{B} - (H + J) - \sqrt{3}\,\mathrm{i}\,(H - J)], \tag{A 9}$$

where

$$H = 2^{2/3}(-N + \sqrt{-4(\mathscr{B}^2 - 3\mathscr{A}\mathscr{C})^3 + N^2})^{1/3},$$
$$J = 4(\mathscr{B}^2 - 3\mathscr{A}\mathscr{C})/H,$$
$$N = 2\mathscr{B}^3 - 9\mathscr{A}\mathscr{B}\mathscr{C} + 27\mathscr{A}^2\mathscr{D}.$$

Once r has been computed from the upstream state using (A 7), (A 8) or (A 9), the complete downstream state (ρ_2, p_2, $\boldsymbol{M}_{S2}$, β_2, θ_2) can be readily computed. First, b is computed using (A 4). An expression for the downstream pressure in terms of r and b can be found by manipulating (2.7) into

$$f_p(r, b) \equiv \frac{p_2}{p_1} = 1 + \gamma M_{S1}^2\left(1 - r - \frac{b^2 - \sin^2(\theta_1)}{2M_{A1}^2}\right). \tag{A 10}$$

The normal component of the downstream Mach number is then simply obtained using

$$M_{S2n} = \sqrt{\frac{r}{f_p(r, b)}}M_{S1n}, \tag{A 11}$$

while the tangential component is obtained by manipulating (2.8) into

$$M_{S2t} = \sqrt{\frac{1}{r f_p(r, b)}}\left(M_{S1t} + M_{S1n}\frac{(b - \sin\theta_1)\cos\theta_1}{M_{A1}^2}\right). \tag{A 12}$$

Finally, β_2 and θ_2 are readily obtained using the definition of b and the fact that B_n is continuous across a shock;

$$\beta_2 = \frac{1}{b^2 + \cos^2(\theta_1)} f_p(r, b)\beta_1, \tag{A 13}$$

$$\sin\theta_2 = \frac{b}{\sqrt{b^2 + \cos^2(\theta_1)}}. \tag{A 14}$$

Appendix B. Governing equations for an MHD expansion fan

The basic equations governing the flow through a centred, steady MHD expansion fan can be obtained by writing (2.1)–(2.2) and (2.4)–(2.5) in cylindrical co-ordinates, then assuming variations occur only with the polar angle φ (Yang & Sonnerup 1976; Krisko & Hill 1991). Further, the flow is assumed to be isentropic; hence, the energy equation is replaced by an entropy equation. Under these assumptions, the governing

https://doi.org/10.1017/S0022112004001880 Published online by Cambridge University Press

equations become

$$\rho u_t + \rho \partial_\varphi u_n + u_n \partial_\varphi \rho = 0, \tag{B 1}$$

$$u_t u_n + u_n \partial_\varphi u_n + \partial_\varphi p/\rho - B_t B_n/\mu_0 \rho + B_t \partial_\varphi B_t/\mu_0 \rho = 0, \tag{B 2}$$

$$u_n^2 - u_n \partial_\varphi u_t - B_n^2/\mu_0 \rho + B_n \partial_\varphi B_t/\mu_0 \rho = 0, \tag{B 3}$$

$$\partial_\varphi p/p - \gamma \partial_\varphi \rho/\rho = 0, \tag{B 4}$$

$$B_t + \partial_\varphi B_n = 0, \tag{B 5}$$

$$B_t \partial_\varphi u_n + u_n \partial_\varphi B_t - B_n \partial_\varphi u_t - u_t \partial_\varphi B_n = 0, \tag{B 6}$$

where $\partial_\varphi \equiv \partial/\partial\varphi$, and the subscripts n and t denote vector components in the φ and r directions, respectively. Equations (B 1)–(B 6) form a system for $\partial_\varphi \rho$, $\partial_\varphi p$, $\partial_\varphi u_t$, $\partial_\varphi u_n$, $\partial_\varphi B_t$ and $\partial_\varphi B_n$. It can be shown that if the determinant of the system is non-zero, only the trivial solution of uniform flow is admissible. Thus, for an MHD expansion fan to be a valid solution, the system must be singular, which requires

$$\frac{u_n^4}{p} - \frac{u_n^2}{\rho}\left(\gamma + \frac{B_n^2}{\mu_0 p} + \frac{B_t^2}{\mu_0 p}\right) + \frac{\gamma B_n^2}{\mu_0 \rho^2} = 0. \tag{B 7}$$

We introduce the following non-dimensional vector to represent the magnetic field:

$$\boldsymbol{K} \equiv \frac{\boldsymbol{B}}{\sqrt{2\mu_0 p}}. \tag{B 8}$$

After non-dimensionalization, (B 1)–(B 6) can be combined to form the following set of differential equations from which pressure has been eliminated (Yang & Sonnerup 1976):

$$\partial_\varphi M_n = -\frac{(\gamma+1)}{2} M_n \frac{\partial_\varphi \rho}{\rho} - M_t, \tag{B 9}$$

$$\partial_\varphi M_t = \left(-\frac{K_t M_n}{K_n M_t} + \frac{1-\gamma}{2} + \frac{\gamma M_n \left(M_n^2 - 1\right)}{2 K_n K_t M_t}\right) M_t \frac{\partial_\varphi \rho}{\rho} + M_n, \tag{B 10}$$

$$\partial_\varphi K_n = -\frac{\gamma K_n}{2} \frac{\partial_\varphi \rho}{\rho} - K_t, \tag{B 11}$$

$$\partial_\varphi K_t = \frac{\gamma}{2}\left(\frac{M_n^2}{K_t^2} - 1 - K_t^{-2}\right) K_t \frac{\partial_\varphi \rho}{\rho} + K_n. \tag{B 12}$$

Here, M denotes the sonic Mach number. By combining the derivative of (B 7),

$$\partial_\varphi \left(M_n^4 - M_n^2\left[1 + \frac{2}{\gamma}\left(K_n^2 + K_t^2\right)\right] + \frac{2}{\gamma} K_n^2\right) = 0,$$

with (B 9)–(B 12), we obtain

$$\frac{\partial_\varphi \rho}{\rho} = \frac{4 M_n^3 M_t - 2 M_n M_t \left[1 + (2/\gamma)\left(K_n^2 + K_t^2\right)\right] + (4/\gamma) K_n K_t}{-2K_n^2 - 2(2+\gamma) M_n^4 + M_n^2\left[3 + (4 + 2/\gamma)\left(K_n^2 + K_t^2\right) + \gamma\right]}. \tag{B 13}$$

The complete solution throughout the expansion fan can be found by numerically integrating (B 9)–(B 13) with respect to φ, then using the isentropic relation to recover the pressure. The domain of integration begins at the leading wavelet of the expansion fan. This wavelet propagates at either the fast or slow MHD characteristic speed with respect to the upstream flow, depending on whether we are considering a fast- or a slow-mode expansion fan. Thus, the angle of the leading wavelet to the upstream

https://doi.org/10.1017/S0022112004001880 Published online by Cambridge University Press

velocity vector, ϕ, must satisfy

$$M_{Fn/SLn}(\phi_{F/SL}) = 0. \tag{B 14}$$

Appendix C. Governing equations for a slow compound wave

For certain shock solutions to the MHD RH relations, it is possible for rarefaction waves to move with the shocks. This can occur for shocks that propagate at the fast characteristic speed and for shocks where the downstream normal flow speed relative to the shock is the slow characteristic speed. When a rarefaction travels immediately upstream or downstream of one of these shocks, the combination is referred to as a *compound wave*. In the context of MHD, these waves were first identified in numerical solutions to the full MHD equations by Wu (1987). In the strongly planar MHD system, Myong & Roe (1997) recommend the use of compound waves as a substitute for $2 \rightarrow 3$ intermediate shocks, which are inadmissible under their viscosity admissibility condition and the evolutionary condition.

The compound wave relevant to this study consists of a $2 \rightarrow 3 = 4$ intermediate shock, for which $u_{n2} = C_{SL2}$, followed immediately downstream by a slow-mode expansion fan. This is the steady two-dimensional analogue of the unsteady one-dimensional slow compound wave referred to as C_1 by Myong & Roe (1997). We will use the same designation for the two-dimensional compound wave.

For a $2 \rightarrow 3 = 4$ intermediate shock to occur, roots B and C of the RH relations must be equal. Comparing (A 8) and (A 9), it is apparent that this implies $H = J$. In terms of the coefficients of (A 6), this can be expressed as

$$\mathscr{D} = \frac{-2\mathscr{B}^3 + 9\mathscr{A}\mathscr{B}\mathscr{C} - 2\mathscr{B}^2\sqrt{\mathscr{B}^2 - 3\mathscr{A}\mathscr{C}} + 6\mathscr{A}\mathscr{C}\sqrt{\mathscr{B}^2 - 3\mathscr{A}\mathscr{C}}}{27\mathscr{A}^2}. \tag{C 1}$$

This relationship must be satisfied by the upstream flow state in order for a C_1 compound wave to be possible. The flow state downstream of a compound wave is computed as follows: as $H = J$ for a $2 \rightarrow 3 = 4$ intermediate shock, the following simplified relationship can be used to compute r:

$$r_{B/C} = -\frac{1}{6\mathscr{A}}(2\mathscr{B} + H). \tag{C 2}$$

After b is computed using (A 4), the remainder of the flow state downstream of the shock may be computed using (A 10)–(A 14). Using this flow state as initial data, the conditions downstream of the compound wave are then found by integrating (B 9)–(B 13) across the expansion-fan portion of the wave.

Appendix D. Matching conditions at the contact discontinuity

The conditions on either side of the shocked contact discontinuity (SC) are computed as follows. First, the conditions upstream of shocks I (denoted with a subscript 0) and TF (denoted with a subscript b) in the reference frame where the intersection point is stationary are computed from the problem parameters using

$$\boldsymbol{U}_0 = (1, 1, M, -M\tan\alpha, \beta, \pi),$$

$$\boldsymbol{U}_b = \left(\eta, 1, \sqrt{\eta}\frac{\cos\left(\frac{1}{2}\pi - \phi_3 + \alpha\right)}{\cos\alpha}M, \sqrt{\eta}\frac{\sin\left(\frac{1}{2}\pi - \phi_3 + \alpha\right)}{\cos\alpha}M, \beta, -\tfrac{1}{2}\pi - \phi_3\right),$$

where $\boldsymbol{U} \equiv (\rho, p, M_{Sn}, M_{St}, \beta, \theta)$ and ϕ_3 is the angle between shock TF and the negative x-axis, as indicated in figure 5, which shows how the various angles and regions of

https://doi.org/10.1017/S0022112004001880 Published online by Cambridge University Press

uniform flow in the problem are designated. θ and the normal and tangential vector components in $\boldsymbol{U}$ are defined with respect to the wave at the downstream boundary of a region.

Next, the conditions downstream of shock I (state 1) are computed. This is done by first computing the normal velocity ratio r_0 across shock I using the appropriate root of the RH relations, root A, B or C. The specifics of which root is appropriate for each of the shocks for a given set of problem parameters will be discussed in §§4 and 5. Once $r_0 = \rho_1^{-1}$ is determined, the remainder of state 1 is computed using (A 4) and (A 10)–(A 14).

In order to compute the conditions across shock RF, the components of $\boldsymbol{M}_{S1}$ normal and tangential to it are computed using

$$\left.\begin{aligned} M'_{Sn} &= M_{Sn}\cos\Delta\phi - M_{St}\sin\Delta\phi, \\ M'_{St} &= M_{Sn}\sin\Delta\phi + M_{St}\cos\Delta\phi, \end{aligned}\right\} \tag{D 1}$$

where the unprimed and primed quantities are defined with respect to upstream and downstream waves, respectively, and $\Delta\phi$ is the angle between the two waves. The vector representing the magnetic field is redefined in the same manner. State 2 downstream of shock RF can then be computed using the RH relations, as for state 1.

If RS is a shock, the procedure used to compute state 2 is repeated to compute state 3 downstream of shock RS. It will be shown in §§4 and 5 that, in some instances, shock RS and/or shock TS is replaced by either a C_1 compound wave, a 180° rotational discontinuity (RD) followed by a slow shock, or an RD followed by a slow-mode expansion fan. Assuming that RS is a C_1 compound wave, the angle between its leading edge and shock RF ($\Delta\phi_c$) must be calculated. This is done by expressing the coefficients in (C 1) in terms of state 2 and $\Delta\phi_c$, then solving this relation numerically. Once $\Delta\phi_c$ is known, equations (D 1) are used to compute the vector components normal and tangential to the leading edge of the compound wave. The procedure outlined in Appendix C is then used to compute the flow-state downstream of the compound wave. These are the conditions to the left of the SC and are referred to as state 3. If, instead, we assume that the RS wave group begins with an RD, an intermediate state denoted with a subscript d must be calculated downstream of the RD. This is done by first calculating the angle between the RD and shock RF, $\Delta\phi_d$. Using the fact that the rotational discontinuity propagates at the upstream intermediate characteristic speed with respect to the flow, it can be shown that

$$\Delta\phi_d = \arctan\left(\frac{\sqrt{2/\gamma}K_{2n} - M_{S2n}}{\sqrt{2/\gamma}K_{2t} - M_{S2t}}\right), \tag{D 2}$$

where the subscripts n and t refer to vector components normal and tangential to shock RF. Once $\Delta\phi_d$ is known, equations (D 1) are used to compute the vector components normal and tangential to the RD. State d is then determined from the RH relations, making use of the fact that for a 180° RD, $r = 1$ and $b = -\sin\theta_1$. If the remainder of the RS wave group is a slow shock, the procedure used to compute state 2 is repeated to compute state 3. Alternatively, if the RS wave group concludes with a slow-mode expansion fan, the next step is to compute the location of the leading wavelet of the fan ϕ_{f1} by solving (B 14). Equations (B 9)–(B 13) are then integrated numerically from ϕ_{f1} to the angle of the last wavelet using state d as the initial conditions. This yields the conditions to the left of the SC.

https://doi.org/10.1017/S0022112004001880 Published online by Cambridge University Press

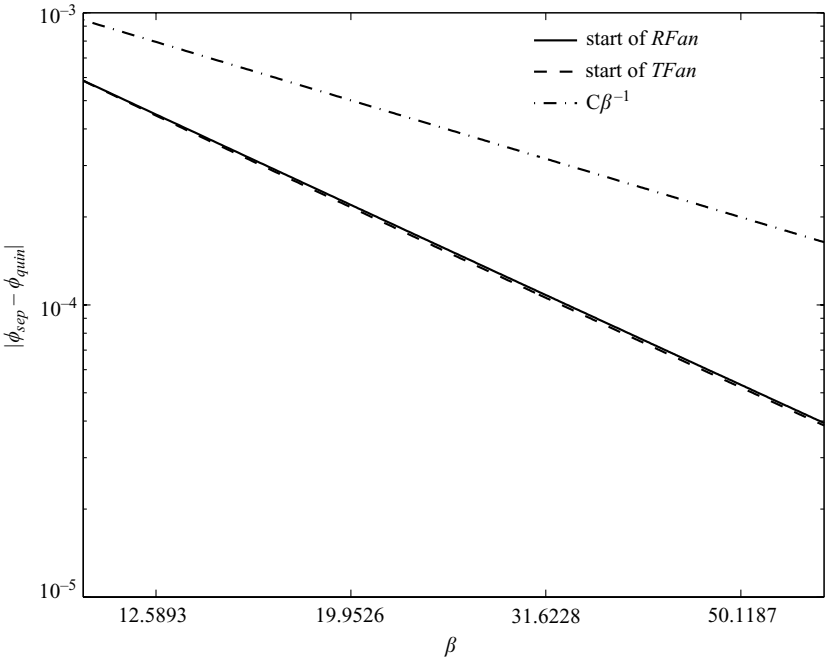


FIGURE 18. Difference between the locations of the leading expansion fan wavelets of *RFan* and *TFan* in the two solutions along Branches I*c* (subscript quin) and I*r* (subscript sep).

The conditions to the right of the SC (state 5) are determined using an analogous procedure. For the proposed wave configuration to be a valid solution of the equations of ideal MHD, states 3 and 5 must satisfy matching conditions (2.11)–(2.15).

Appendix E. Equivalence of leading-order asymptotic quintuple and septuple-point solutions

We present the following argument that the leading-order asymptotic solution to the shock refraction problem is the large β limit of both the quintuple-point and septuple-point solutions; upstream of the $2 \to 3 = 4$ intermediate shocks in the quintuple-point solution and the RDs in the septuple-point solution, our results indicate that the primitive variables can be expressed as

$$\rho(\phi;\varepsilon) = \rho^{(0)}(\phi) + \varepsilon\rho^{(1)}(\phi) + O(\varepsilon^2),$$
$$p(\phi;\varepsilon) = p^{(0)}(\phi) + \varepsilon p^{(1)}(\phi) + O(\varepsilon^2),$$
$$u_n(\phi;\varepsilon) = \varepsilon u_n^{(1)}(\phi) + O(\varepsilon^2),$$
$$u_t(\phi;\varepsilon) = u_t^{(0)}(\phi) + \varepsilon u_t^{(1)}(\phi) + O(\varepsilon^2),$$
$$\boldsymbol{B}(\phi;\varepsilon) = \varepsilon \boldsymbol{B}^{(1)}(\phi) + O(\varepsilon^2).$$

Substituting these expansions into the RH relations and collecting terms of the same order, it can be shown that $\rho^{(0)}$, $p^{(0)}$, $u_n^{(1)}$, $u_t^{(0)}$ and $B_n^{(1)}$ are constant across both the $2 \to 3 = 4$ intermediate shocks and RDs in our solutions for small ε. Thus, these discontinuities do not affect the boundary conditions for (7.6)–(7.10) and are omitted from the leading-order solution. From figure 18, it can be seen that the difference between the locations of the leading expansion fan wavelets in the two solutions

https://doi.org/10.1017/S0022112004001880 Published online by Cambridge University Press

is less than $O(\varepsilon^2)$, which also has no effect on the boundary conditions for (7.6)–(7.10). These two facts, combined with the observation that outside of the inner layer, both solutions converge to the hydrodynamic triple-point as $\beta^{-1/2}$, imply that the leading-order asymptotic solution is the large β limit of both the quintuple-point and septuple-point solutions.

REFERENCES

Akhiezer, A. I., Liubarskii, G. I. & Polovin, R. V. 1959 The stability of shock waves in magnetohydrodynamics. *Sov. Phys. J. Exp. Theor. Phys.* **8**, 507–511.

Bestman, A. R. 1975 Confluence of three shock waves for transverse shocks and shocks in an aligned MHD field. *J. Plasma Phys.* **13**, 107–125.

Falle, S. A. E. G. & Komissarov, S. S. 2001 On the inadmissibility of non-evolutionary shocks. *J. Plasma Phys.* **65**, 29–58.

Jeffrey, A. & Taniuti, T. 1964 *Nonlinear Wave Propagation*. Academic.

Kennel, C. F., Blandford, R. D. & Coppi, P. 1989 MHD intermediate shock discontinuities. Part 1. Rankine–Hugoniot conditions. *J. Plasma Phys.* **42**, 299–319.

Krisko, P. H. & Hill, T. W. 1991 Two-dimensional model of a slow-mode expansion fan at Io. *Geophys. Res. Lett.* **18**, 1947–1950.

Liberman, M. A. & Velikhovich, A. L. 1986 *Physics of Shock Waves in Gases and Plasmas*. Springer.

Myong, R. S. & Roe, P. L. 1997 Shock waves and rarefaction waves in magnetohydrodynamics. Part 2. The MHD system. *J. Plasma Phys.* **58**, 521–552.

Ogawa, H. & Fujiwara, T. 1996 Analyses of three shock interactions in magnetohydrodynamics: aligned-field case. *Phys. Plasmas* **3**, 2924–2938.

Polovin, R. V. & Demutskii, V. P. 1990 *Fundamentals of Magnetohydrodynamics*. Consultants Bureau, New York.

Samtaney, R. 2003 Suppression of the Richtmyer–Meshkov instability in the presence of a magnetic field. *Phys. Fluids* **15**, L53–L56.

Sutton, G. W. & Sherman, A. 1965 *Engineering Magnetohydrodynamics*. McGraw-Hill.

Torrilhon, M. 2003*a* Non-uniform convergence of finite volume schemes for Riemann problems of ideal magnetohydrodynamics. *J. Comput. Phys.* **192**, 73–94.

Torrilhon, M. 2003*b* Uniqueness conditions for Riemann problems of ideal magnetohydrodynamics. *J. Plasma Phys.* **69**, 253–276.

Wu, C. C. 1987 On MHD intermediate shocks. *Geophys. Res. Lett.* **14**, 668–671.

Wu, C. C. 1990 Formation, structure and stability of MHD intermediate shocks. *J. Geophys. Res.* **95**, 8149–8175.

Wu, C. C. 1995 Magnetohydrodynamic Riemann problem and the structure of the magnetic reconnection layer. *J. Geophys. Res.* **100**, 5579–5598.

Yang, C. K. & Sonnerup, B. U. Ö. 1976 Compressible magnetic field reconnection: a slow wave model. *Astrophys. J.* **206**, 570–582.

https://doi.org/10.1017/S0022112004001880 Published online by Cambridge University Press